

Dissipationless transport signature of topological nodal lines

Arthur Veyrat,^{1,2,3} Klaus Koepf, ^{1,2} Louis Veyrat,^{1,2,4} Grigory Shipunov,^{1,2} Saicharan Aswartham,^{1,2} Jiang Qu,^{1,2} Ankit Kumar,^{1,2} Michele Ceccardi,^{5,6} Federico Cagliaris,⁶ Nicolás Pérez Rodríguez,^{1,2} Romain Giraud,^{1,2,7} Bernd Büchner,^{1,2,8} Jeroen van den Brink,^{1,2,8} Carmine Ortix,^{9,*} and Joseph Dufouleur^{1,2,10,†}

¹*Leibniz Institute for Solid State and Materials Research (IFW Dresden), Helmholtzstraße 20, D-01069 Dresden, Germany*

²*Würzburg-Dresden Cluster of Excellence ct.qmat, Dresden, Germany*

³*Laboratoire de Physique des Solides (LPS Orsay), 510 Rue André Rivière, 91400 Orsay, France*

⁴*CNRS, Laboratoire National des Champs Magnétiques Intenses, Université Grenoble-Alpes, Université Toulouse 3, INSA-Toulouse, EMFL, 31400 Toulouse, France*

⁵*Department of Physics, University of Genoa, 16146 Genoa, Italy*

⁶*CNR-SPIN Institute, 16152 Genoa, Italy*

⁷*Université Grenoble Alpes, CNRS, CEA, Grenoble-INP, Spintec, F-38000 Grenoble, France*

⁸*Department of Physics, TU Dresden, D-01062 Dresden, Germany*

⁹*Dipartimento di Fisica “E. R. Caianiello”, Università di Salerno, IT-84084 Fisciano (SA), Italy*

¹⁰*Center for Transport and Devices, TU Dresden, D-01069 Dresden, Germany*

Topological materials, such as topological insulators or semimetals, usually not only reveal the nontrivial properties of their electronic wavefunctions through the appearance of stable boundary modes [1], but also through very specific electromagnetic responses [2]. The anisotropic longitudinal magnetoresistance of Weyl semimetals [3], for instance, carries the signature of the chiral anomaly of Weyl fermions. However for topological nodal line (TNL) semimetals [4, 5] – materials where the valence and conduction bands cross each other on one-dimensional curves in the three-dimensional Brillouin zone – such a characteristic has been lacking. Here we report the discovery of a peculiar charge transport effect generated by TNLs: a dissipationless transverse signal in the presence of coplanar electric and magnetic fields [6, 7], which originates from a Zeeman-induced conversion of TNLs into Weyl nodes under infinitesimally small magnetic fields. We evidence this dissipationless topological response in trigonal PtBi₂ persisting up to room temperature, and unveil the extensive TNLs in the band structure of this non-magnetic material. These findings provide a new pathway to engineer Weyl nodes by arbitrary small magnetic fields and reveal that bulk topological nodal lines can exhibit non-dissipative transport properties.

The electronic band structure of a bulk material can feature isolated degeneracy points where electronic states with different spin, orbital or sublattice quantum number possess same energy and crystalline momentum \mathbf{k} . In materials lacking either inversion or time-reversal symmetry, such degeneracies can be simply twofold while occurring at generic points in the three-dimensional Brillouin zone. The electronic bands in the vicinity of the

nodes then generally resembles the energetic dispersion of massless relativistic particles governed by the Weyl equation [8]. Weyl nodes represent monopoles of the Berry flux and are thus characterized by a well-defined topological charge. This non-trivial bulk topology is manifested in a very specific spectroscopic signature: the presence of surface Fermi arcs connecting Weyl points with opposite chirality [9, 10]. The characteristic electromagnetic response of Weyl quasiparticles is instead connected to their chiral anomaly [11, 12]. This causes a strong in-plane anisotropic magnetoconductivity that can be directly probed through measurements of the planar Hall effect (PHE) [3, 13, 14]: the appearance, in the presence of coplanar electric and magnetic fields, of a transverse voltage with π -periodic angular dependence. Weyl quasiparticles may also be evidenced in transport experiments through other effects, such as the unconventional Hall effect [15].

Point-group symmetries can also stabilize twofold degenerate closed lines in the three-dimensional Brillouin zone. When appearing at mirror invariant planes such nodal lines are characterized by a bulk \mathbb{Z}_2 topological invariant [5, 16]. Although they are often accompanied by “drumhead” surface states [17–19], topological nodal lines (TNLs) lack a genuine bulk-boundary correspondence: the relevant surfaces naturally break the protecting mirror symmetry [20]. Additionally, some electromagnetic responses characteristic of TNL-semimetals have been identified, but only in specific cases, such as for instance in the quantum limit [21], making the physical consequences of the bulk topology completely hidden. Here, we unveil a peculiar charge transport effect associated with mirror symmetry-protected TNLs in trigonal crystals: an anomalous planar Hall effect (APHE) that is odd in magnetic field, does not contribute to the dissipated power [6], and is measurable in the linear transport regime. We identify trigonal-PtBi₂ as an ideal material platform because of the presence of a large number of TNLs on its three vertical mirror planes that makes the anomalous planar Hall effect particularly robust and sur-

* cortix@unisa.it

† j.dufouleur@ifw-dresden.de

viving up to room temperature.

TOPOLOGICAL NODAL LINE CONVERSION IN MAGNETIC FIELD

In low-dimensional systems, such as $\text{LaAlO}_3/\text{SrTiO}_3$ oxide interfaces, the occurrence of an APHE has been reported and is due to a Zeeman-induced modification of local concentrations of the out-of-plane Berry curvature, which, when integrated over momenta, becomes non-vanishing [22]. An APHE has also been reported in VS_2 -VS heterostructures [23]. The mechanism we find to be at work in TNLs is completely different in nature. It is caused by a Zeeman-induced conversion of TNLs into Weyl nodes that generalizes the fusion of Weyl nodes into nodal lines predicted to occur in mirror-symmetric systems [16]. The important point is that magnetic fields that break the mirror symmetry protecting the TNLs lead to a nonlocal conversion of the TNL into Weyl nodes of opposite chirality, meaning that they are separated in momentum space by a vector that has components parallel to the mirror plane. The extraordinary feature of this k -space separation in momentum space is that it survives even for infinitesimally small magnetic field and can be as large as the diameter of the TNL. This conversion and its properties can be qualitatively captured using a simple two-band low-energy model (see SM). This generally induces large momentum regions of non-zero Chern number, thus generating an anomalous planar Hall effect (APHE) already at infinitesimal magnetic field, with a much larger amplitude than that which would be obtained solely from the Zeeman-induced displacement of Weyl nodes (see SM). Consider for simplicity a single pair of TNLs related to each other by time-reversal symmetry and protected by a vertical mirror plane, which, without loss of generality, we set as \mathcal{M}_x (see Fig. 1.a). With an infinitesimally small magnetic field along the \hat{y} direction, the TNLs convert into two field-induced pairs of Weyl nodes, each of which has a separation in k_z comparable to the TNL dimension, generating a dissipationless (i.e. without diagonal components) antisymmetric Hall conductance σ_{yx} (i.e. an APHE). The system can be viewed in fact as a collection of two dimensional $\{k_x, k_y\}$ insulating layers [?] parameterized by k_z and characterized by a local Chern number $c(k_z)$ (see Fig. 1.a) that is changed by the topological charge of each Weyl node. The non-local Zeeman-induced conversion of the TNLs into Weyl nodes then leads to a net $\sigma_{yx} = \int c(k_z) dk_z$ and to Hall voltages that lie in the same plane as the applied current and the external magnetic field, precisely in a configuration where the conventional Hall effect is absent. Such APHE thus represents a characteristic electromagnetic response of TNLs.

Additionally, Onsager's relations [?] enforce the transversal APHE conductance to be odd under a magnetic field reversal and thus compatible only with an out-of-plane threefold rotational symmetry (see Fig. 1.b).

This property, along with its non-dissipative character, makes the APHE experimentally distinguishable from a planar Hall effect. First, a PHE, such as that associated with the Berry curvature of the Weyl nodes, is characterized by a π -periodic oscillation of both the longitudinal R_{xx} and transverse resistance R_{yx} , when the magnetic field is rotated in-plane while keeping the current direction fixed, with a $\pi/4$ offset between them (see Fig. 1.b and Methods) [3, 13]. The longitudinal resistance R_{xx} is moreover maximized when magnetic field and current are aligned, while the transverse resistance R_{yx} vanishes in this configuration. As a result, a two-fold symmetric PHE aligned with current direction can easily be disentangle from a threefold-symmetric APHE aligned with crystalline axes (see Fig. 1.b). More importantly, the APHE is non-dissipative, i.e it is not associated with any corresponding longitudinal signal. This allows to distinguish it unambiguously from any potential three-fold symmetric PHE due to magneto-crystalline anisotropies, which would be associated with a corresponding AMR.

ANOMALOUS PLANAR HALL EFFECT

We now show that both these effects can be probed in the layered van der Waals material PtBi_2 , that has recently been characterized as a non-magnetic type I Weyl semimetal. PtBi_2 also exhibits sub-Kelvin 2D-superconductivity and a BKT transition in nanostructures [24], as well as higher-temperature surface superconductivity [25] with superconducting topological Fermi arcs [10]. The crystallographic point group symmetry of PtBi_2 is \mathcal{C}_{3v} that is comprised of a three-fold axis and three vertical mirror planes \mathcal{M} (Fig. 1.c) [26], and is compatible with the appearance of an APHE. When an in-plane magnetic field is perpendicular to a mirror plane, the anomalous Hall conductivity (AHC) σ_{yx} must vanish. Conversely, when the field is parallel to a mirror plane, σ_{yx} is maximal [6]. This results in a $2\pi/3$ periodic angular dependence (see Fig. 1.c) that can be detected in practice with magnetotransport measurements.

We focus our study on a 70nm thick nanostructure (see magnetotransport measurement schematic in Fig. 1.d) investigated up to 14T, and temperatures from 5K up to 300K (another structure showed similar behavior, see Supplementary Material). The results are shown in Fig. 2. First, in exfoliated nanostructures of PtBi_2 , we systematically observed a PHE. At $T = 100$ K and $B = 14$ T, a pronounced π -periodic oscillation is clearly visible in both R_{xx} and R_{yx} (Fig. 2.a), with the expected $\pi/4$ angular shift between them (Fig. 2.b). The PHE is already visible at magnetic fields as low as 1 T (see Supplementary Materials Fig. S2). The angular positions of the maxima of R_{xx} are consistent with the expected current orientation in the sample (see Methods). The PHE is very robust with temperature, and for $B = 14$ T it can be evidenced up to room temperature (Fig. 2.c). The presence of a strong PHE in the non-magnetic PtBi_2

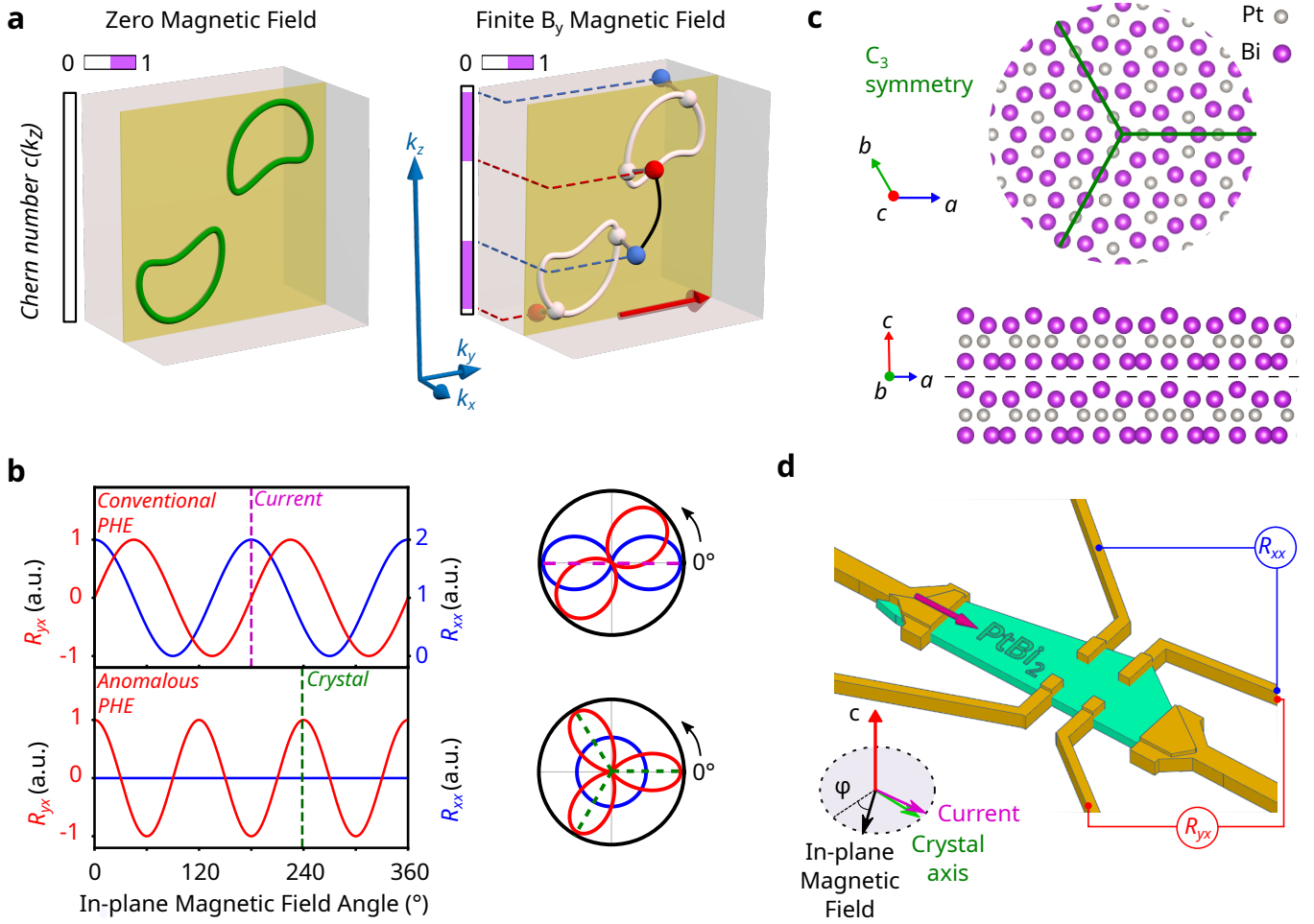


FIG. 1. **Anomalous planar Hall effects in PtBi₂.** **a:** Generation of an anomalous Hall conductance in nodal line semimetal systems. In a nodal line semimetal, the nodal lines do not contribute to the Chern number at zero magnetic field (left panel). Under a finite external magnetic field (right panel, red arrow), the nodal lines split into pairs of Weyl nodes of opposite chiralities. These pairs can appear anywhere on the nodal lines, including with a significant k_z separation. This leads to potential large k_z ranges of non-zero $c(k_z)$, inducing a large AHC at finite field. **b:** Typical angular dependence of the conventional (top panel) and anomalous (bottom panel) planar Hall effects, in Cartesian (left) and polar (right) coordinates. For the conventional PHE, both the longitudinal (anisotropic magnetoresistance, R_{xx} , blue) and transverse (planar Hall effect, R_{yx} , red) resistances exhibit a π -periodic angular dependence, with a $\pi/4$ -offset between them. The origin of the oscillation is set by the direction of the electric field (current). For the APHE, the angular dependence is $2\pi/3$ -periodic, with origin set by the crystal directions, and is not associated with any AMR. **c:** Crystal structure of trigonal-PtBi₂, with layered nature and in-plane C_3 -symmetry highlighted. **d:** Sample configuration. The angle φ refers to the orientation of the in-plane magnetic field \mathbf{B} .

reveals the large BC present in the material, giving significant experimental indications of its Weyl nature, and confirming predictions from previous band structure calculations [24].

The main experimental result of this work is the evidence of an APHE in our measurements, which appears as a small deviation from the PHE in Fig. 2.a-c. In order to evidence the APHE in our data, we remove a π - and 2π -periodic background from each measurement (in red in Fig. 2.a,b, and Supplementary sec. S2). Removing each signal separately would be similar to antisymmetrizing (resp. symmetrizing) the data in magnetic field, albeit with more control over exactly which terms are removed. The resulting residues are depicted in Fig.

2.d-f. At 14T, $2\pi/3$ -periodic oscillations, which contrary to the standard PHE signal are antisymmetric in B , are clearly visible in the transverse resistance residues ΔR_{yx} at 100K (Fig. 2.d,e) and can be fitted with cosine fits (Fig. 2.e, in green). This $2\pi/3$ -periodic signal appears above $B = 4$ T, at a constant angular position, and its amplitude increases with magnetic field (Supplementary sec. S4). Importantly, no associated $2\pi/3$ -periodic signal is visible in the longitudinal resistance residues ΔR_{xx} , up to the highest fields and down to the lowest temperatures (Supplementary Fig. S4). This lack of longitudinal component is critical in distinguishing the dissipationless APHE from any conventional, dissipative PHE which would necessarily be associated with an AMR. Remark-

ably, the APHE is very robust in temperature, as the oscillations remain visible from 5K up to room temperature, as shown in Fig. 2.f.

The field and temperature dependence of the APHE signal obtained from the cosine fits are presented in Fig. 2.g,h. At 5K, the APHE signal is visible above 4T, and increases linearly with field. This fit yields a critical magnetic field $B_c \sim 2.8$ T for the appearance of an APHE. At 14T, the APHE signal remains constant in temperature below 20K, similar to the PHE and the longitudinal resistance (see Supplementary sec. S3). Above this temperature, it decreases following an exponential decay law $A^{APHE}(T) - A^{APHE}(T=0) \propto e^{-k_B(T-T_c)/\Delta}$ with $T_c \sim 30$ K and an energy scale $\Delta \sim 6$ meV. The existence of an onset field for the APHE could be explained by the fact that, while the TNLs are already topologically gapped at infinitesimal fields, the APHE would only become visible when the gap of the TNL exceeds the thermal activation energy. Similarly, the exponential decay of the signal in temperature could come from thermal activation through the TNL gap opened by the magnetic field. This is supported by the temperature shift on the onset field evidenced in sample D3 (see Fig. S8). In this case, the energy scale of the decay, Δ , would be linked to the gap of the TNLs.

TOPOLOGICAL NODAL LINES IN PtBi₂ FROM DFT

We next demonstrate that the APHE experimentally observed originates from the presence of TNLs in PtBi₂ by performing full-relativistic electronic band structure calculations, with and without magnetic field. In the absence of Zeeman coupling the material features 3 groups of Weyl nodes, which, due to the concomitant presence of time-reversal symmetry and the threefold rotation symmetry, all come with multiplicity twelve. These groups of Weyl nodes appear above the Fermi energy, with the one lowest in energy being at around 45.3 meV above E_F , in agreement with a previous study [24]. In each of these groups pairs of Weyl nodes of opposite chirality are connected by a vector perpendicular to the mirror plane. The presence of in-plane magnetic field leads to a movement of the Weyl nodes in all momentum directions due to the low residual symmetry: the system possesses at most a vertical $\mathcal{M}' = \mathcal{M} \times \Theta$ symmetry (with Θ time-reversal) when the magnetic field is parallel to the mirror plane \mathcal{M} . However, the Weyl node displacement is proportional to the strength of the applied magnetic field, and remains relatively small at laboratory-accessible fields. The resulting anomalous planar Hall conductance from this displacement is therefore expected to be vanishingly small.

The situation is completely different for the three pairs of nodal loops revealed by our calculations, which lie in the vertical mirror planes of PtBi₂ and are reminiscent of nodal chain semimetals [16]. An infinitesimal mag-

netic field leads to the conversion of the TNLs, each into 6 Weyl nodes [see Fig. 3.a]. Since in PtBi₂ the degeneracy loops do not occur at fixed energies, these Zeeman-induced Weyl nodes form different groups that are separated in energy – we remark that one of these groups has a complex evolution as the magnetic field is increased as it directly combines with one of the preexisting twelvefold Weyl node groups at $B = 0$ (see Supplemental Material). For a magnetic field parallel to one mirror plane each of these groups is sixfold, with pairs of opposite chirality related by the combined \mathcal{M}' symmetry. This immediately implies that an isolated group yields a sizable contribution to the anomalous planar Hall conductance. The latter can be computed in an "ideal" case by simply assuming that the Weyl nodes are all at the Fermi level, in which case each Weyl node provides a unit change to the Chern number of the insulating (k_x, k_y) layers. The distribution of the Weyl nodes in two trios (see Fig. 3.b) at nearly opposite values of k_z demonstrates that a large contribution to the anomalous planar Hall conductance can be expected from the sixfold groups of Zeeman-induced Weyl nodes. This is verified by a direct calculation of the local Chern number of the full system assuming, as before, all Weyl nodes are at the Fermi energy and a Zeeman energy $E_Z = 14$ meV from an applied magnetic field parallel to one of the vertical mirror planes of the material (see Fig. 3.c, in green). We note that E_Z was chosen at such a value for numerical resolutions purposes, and does not correspond to our experimental conditions. As expected, the twelvefold groups of precursive Weyl nodes do not give a large contribution to the anomalous planar Hall conductance.

We have also performed realistic calculations assuming that bands are filled with a Fermi level set at the energy of the Weyl nodes group at 45.3 meV above the non-magnetic E_F (black line in Fig. 3.c). We find that the local Chern signal (see Supplemental Material) of the twelvefold groups is washed out whereas the jumps due to the sixfold groups originating from the conversion of the TNLs are smoothed. However, the realistic contribution to the anomalous planar Hall conductance (red line in Fig. 3.c) is not only due to these TNLs but also derives from the existence of additional nodal lines (see Supplemental Material) that we find in lower valence bands and also undergo conversion into Weyl nodes in the presence of planar magnetic fields. This further demonstrates that the anomalous planar Hall conductance of PtBi₂ is a direct electromagnetic response of TNLs.

DISCUSSION AND OUTLOOKS

To sum up, we have demonstrated that 3D nanostructures of the non-magnetic 3D Weyl semimetal PtBi₂ exhibit, beyond a conventional PHE, a very robust APHE with a signature $2\pi/3$ -periodic oscillation in ΔR_{yx} and an absent dissipative signal in ΔR_{xx} . We have shown that this APHE originates from previously unidentified

topological nodal lines in PtBi₂'s band structure, through a non-local conversion to Weyl nodes under a magnetic field. This mechanism can be generally used to engineer Weyl nodes in materials featuring mirror symmetry-protected nodal lines by means of arbitrary small magnetic fields. Our observations also establish the anomalous planar Hall effect as an efficient magneto-transport tool to reveal the presence of TNLs in trigonal semimet-

als, which could so far only be characterized through spectroscopy measurements. Demonstrating the presence of topological features through transport is especially interesting in PtBi₂, where 2D superconductivity was recently reported [24], and a recent ARPES study further found the superconducting weight to be localised on the topological Fermi arcs [10], opening perspectives for possible topological superconductivity.

-
- [1] M. Z. Hasan and C. L. Kane, *Rev. Mod. Phys.* **82**, 3045 (2010).
- [2] X.-L. Qi and S.-C. Zhang, *Rev. Mod. Phys.* **83**, 1057 (2011).
- [3] S. Nandy, G. Sharma, A. Taraphder, and S. Tewari, *Physical Review Letters* **119**, 1 (2017).
- [4] A. A. Burkov, M. D. Hook, and L. Balents, *Phys. Rev. B* **84**, 235126 (2011).
- [5] C. Fang, Y. Chen, H.-Y. Kee, and L. Fu, *Phys. Rev. B* **92**, 081201 (2015).
- [6] R. Battilomo, N. Scopigno, and C. Ortix, *Physical Review Research* **3**, 1 (2021).
- [7] J. H. Cullen, P. Bhalla, E. Marcellina, A. R. Hamilton, and D. Culcer, *Phys. Rev. Lett.* **126**, 256601 (2021).
- [8] N. P. Armitage, E. J. Mele, and A. Vishwanath, *Reviews of Modern Physics* **90**, 15001 (2018), arXiv:1705.01111.
- [9] X. Wan, A. M. Turner, A. Vishwanath, and S. Y. Savrasov, *Physical Review B - Condensed Matter and Materials Physics* **83**, 1 (2011).
- [10] A. Kuibarov, O. Suvorov, R. Vocaturo, A. Fedorov, R. Lou, L. Merkwitz, V. Voroshnin, J. I. Facio, K. Koepnik, A. Yaresko, G. Shipunov, S. Aswartham, J. V. D. Brink, B. Büchner, and S. Borisenko, *Nature* **626**, 294 (2024).
- [11] H. B. Nielsen and M. Ninomiya, *Physics Letters B* **130**, 389 (1983).
- [12] D. T. Son and B. Z. Spivak, *Physical Review B - Condensed Matter and Materials Physics* **88**, 1 (2013), arXiv:1206.1627.
- [13] A. A. Burkov, *Physical Review B* **96**, 041110 (2017).
- [14] N. Kumar, S. N. Guin, C. Felser, and C. Shekhar, *Physical Review B* **98**, 1 (2018), arXiv:1711.04133.
- [15] J. Ge, D. Ma, Y. Liu, H. Wang, Y. Li, J. Luo, T. Luo, Y. Xing, J. Yan, D. Mandrus, H. Liu, X. C. Xie, and J. Wang, *Natl. Sci. Rev.* **7**, 1879 (2020).
- [16] X.-Q. Sun, S.-C. Zhang, and T. Bzdušek, *Phys. Rev. Lett.* **121**, 106402 (2018).
- [17] H. Huang, J. Liu, D. Vanderbilt, and W. Duan, *Phys. Rev. B* **93**, 201114 (2016).
- [18] G. Bian, T.-R. Chang, H. Zheng, S. Velury, S.-Y. Xu, T. Neupert, C.-K. Chiu, S.-M. Huang, D. S. Sanchez, I. Belopolski, N. Alidoust, P.-J. Chen, G. Chang, A. Bansil, H.-T. Jeng, H. Lin, and M. Z. Hasan, *Phys. Rev. B* **93**, 121113 (2016).
- [19] Y.-H. Chan, C.-K. Chiu, M. Y. Chou, and A. P. Schnyder, *Phys. Rev. B* **93**, 205132 (2016).
- [20] G. Bian, T.-R. Chang, R. Sankar, S.-Y. Xu, H. Zheng, T. Neupert, C.-K. Chiu, S.-M. Huang, G. Chang, I. Belopolski, D. S. Sanchez, M. Neupane, N. Alidoust, C. Liu, B. Wang, C.-C. Lee, H.-T. Jeng, C. Zhang, Z. Yuan, S. Jia, A. Bansil, F. Chou, H. Lin, and M. Z. Hasan, *Nat Commun* **7**, 10556 (2016).
- [21] Y. Wang, T. Bömerich, J. Park, H. F. Legg, A. A. Taskin, A. Rosch, and Y. Ando, *Phys. Rev. Lett.* **131**, 146602 (2023).
- [22] E. Lesne, Y. G. Sağlam, R. Battilomo, M. T. Mercaldo, T. C. van Thiel, U. Filippozzi, C. Noce, M. Cuoco, G. A. Steele, C. Ortix, and A. D. Caviglia, *Nat. Mater.* **22**, 576 (2023).
- [23] J. Zhou, W. Zhang, Y.-C. Lin, J. Cao, Y. Zhou, W. Jiang, H. Du, B. Tang, J. Shi, B. Jiang, X. Cao, B. Lin, Q. Fu, C. Zhu, W. Guo, Y. Huang, Y. Yao, S. S. P. Parkin, J. Zhou, Y. Gao, Y. Wang, Y. Hou, Y. Yao, K. Suenaga, X. Wu, and Z. Liu, *Nature* **609**, 46 (2022).
- [24] A. Veyrat, V. Labracherie, D. L. Bashlakov, F. Caglieris, J. I. Facio, G. Shipunov, T. Charvin, R. Acharya, Y. Naidyuk, R. Giraud, J. Van Den Brink, B. Büchner, C. Hess, S. Aswartham, and J. Dufouleur, *Nano Lett.* **23**, 1229 (2023).
- [25] S. Schimmel, Y. Fasano, S. Hoffmann, J. Puig, G. Shipunov, D. Baumann, S. Aswartham, B. Büchner, and C. Hess, arXiv:2302.08968 10.48550/arXiv.2302.08968 (2023), arXiv:2302.08968 [cond-mat].
- [26] G. Shipunov, I. Kovalchuk, B. R. Piening, V. Labracherie, A. Veyrat, D. Wolf, A. Lubk, S. Subakti, R. Giraud, J. Dufouleur, S. Shokri, F. Caglieris, C. Hess, D. V. Efremov, B. Büchner, and S. Aswartham, *Physical Review Materials* **4**, 124202 (2020), arXiv:2002.03976.
- [27] K. Koepnik and H. Eschrig, *Phys. Rev. B* **59**, 1743 (1999).
- [28] J. P. Perdew, K. Burke, and M. Ernzerhof, *Phys. Rev. Lett.* **77**, 3865 (1996).
- [29] T. Fukui, Y. Hatsugai, and H. Suzuki, *J. Phys. Soc. Jpn.* **74**, 1674 (2005).
- [30] A. A. Burkov, *Phys. Rev. Lett.* **113**, 187202 (2014).
- [31] L. Xing, R. Chapai, R. Nepal, and R. Jin, *npj Quantum Materials* **5**, 10.1038/s41535-020-0213-9 (2020).

ACKNOWLEDGMENTS

A.V. acknowledges funding from the European Research Council (ERC) under the European Union's Horizon 2020 research and innovation program (grant Ballistop agreement no. 833350). S.A. acknowledges the financial support of (DFG) through the grant AS 523/4-1. C.O. acknowledges support from the MAECI project "ULTRAQMAT". L.V. was supported by the Leibniz Association through the Leibniz Competition. This

work was supported by the Deutsche Forschungsgemeinschaft (DFG, German Research Foundation) through the Sonderforschungsbereich SFB 1143 and under Germany's Excellence Strategy through the Würzburg-Dresden Cluster of Excellence on Complexity and Topology in Quantum Matter – *ct.qmat* (EXC 2147, project-ids 390858490 and 392019).

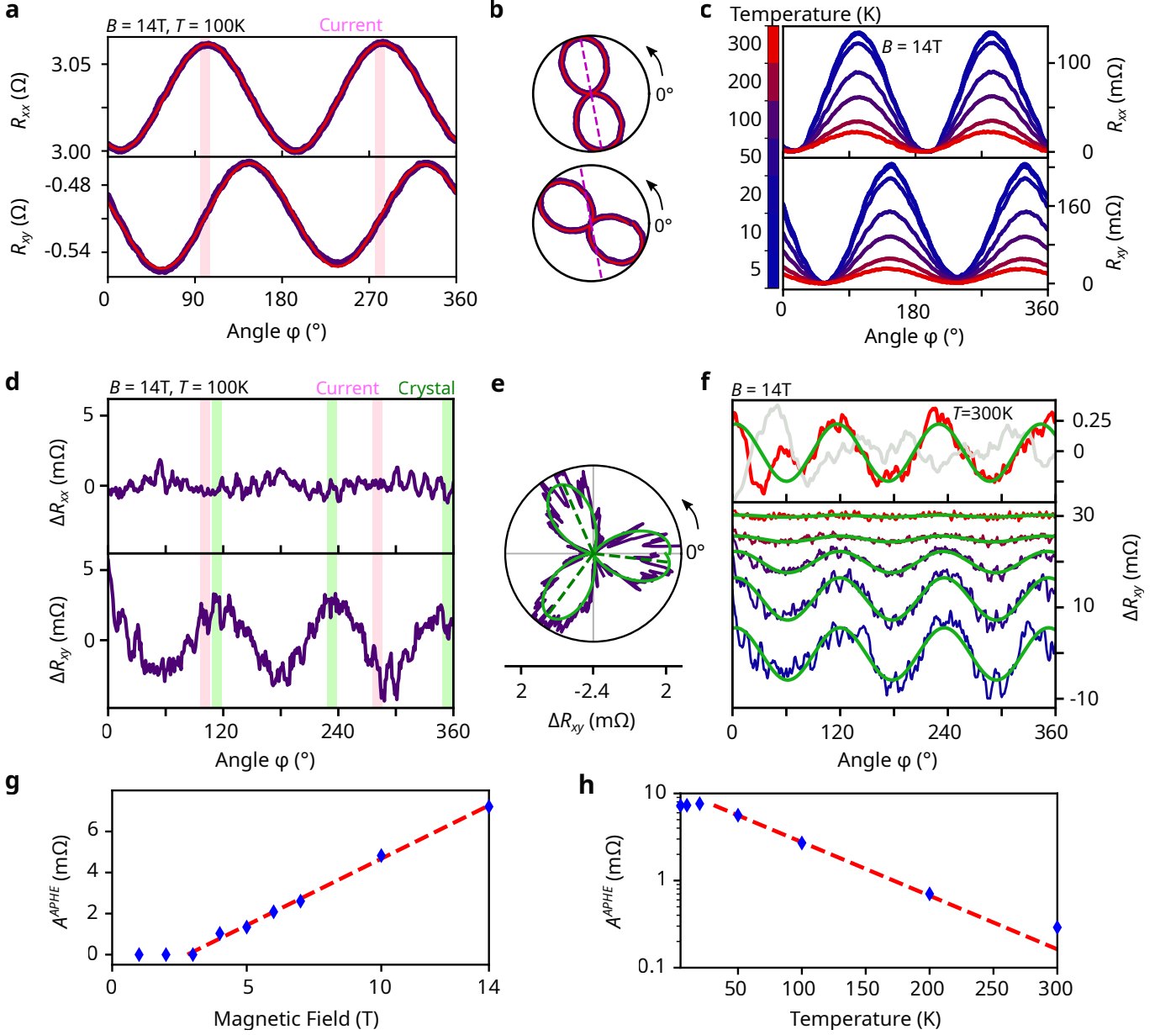


FIG. 2. Standard and Anomalous Planar Hall effect in PtBi₂. **a,b:** Angular dependence of R_{xx} and R_{yx} at 14T, 100K in cartesian (**a**) and polar coordinates (**b**). The fits with Equation 1 (Methods) are shown in red in **a** and **b**. The radial axis has the same range as in **a**. The pink bars in **a** and pink dashed line in **b** show the current direction estimated from the fits, with a $\pm 5^\circ$ width. **c:** Angular dependence of R_{xx} and R_{yx} at different temperatures from 5K to 300K, at 14T. The curves are vertically shifted for clarity. **d,e:** Angular dependence of the residues ΔR_{xx} and ΔR_{yx} from the data in **a** after a background removal (see Supplementary sec. S2), in cartesian (**d**) and polar coordinates (**e**). A $2\pi/3$ -periodic signal is clearly visible in ΔR_{yx} . The pink and green bars show the previously estimated current direction and the crystal direction estimated from the fits to Supplementary Materials eq. S5, respectively, with a $\pm 5^\circ$ width. In **e**, the fit to Supplementary Materials eq. S5 is shown in green. **f:** Bottom: angular dependence of ΔR_{yx} at 14T for $T = 20\text{K}, 50\text{K}, 100\text{K}, 200\text{K}$ and 300K, with fits to Supplementary Materials eq. S5 shown in green. The curves are vertically shifted for clarity. Top: Angular dependence of ΔR_{yx} at 14T, 300K, with fit in green. The 300K data was smoothed over 31° for visibility. The corresponding ΔR_{xx} signal is plotted in grey line with the same scale for comparison, and shows no visible periodic signal. **g:** Field dependence of the APHE amplitude A^{APHE} , showing a linear dependence above $B_c \sim 2.8$ T. **h:** Temperature dependence of A^{APHE} , showing an exponential decay above $T_c \sim 30$ K, with an energy scale $\Delta \sim 6$ meV.

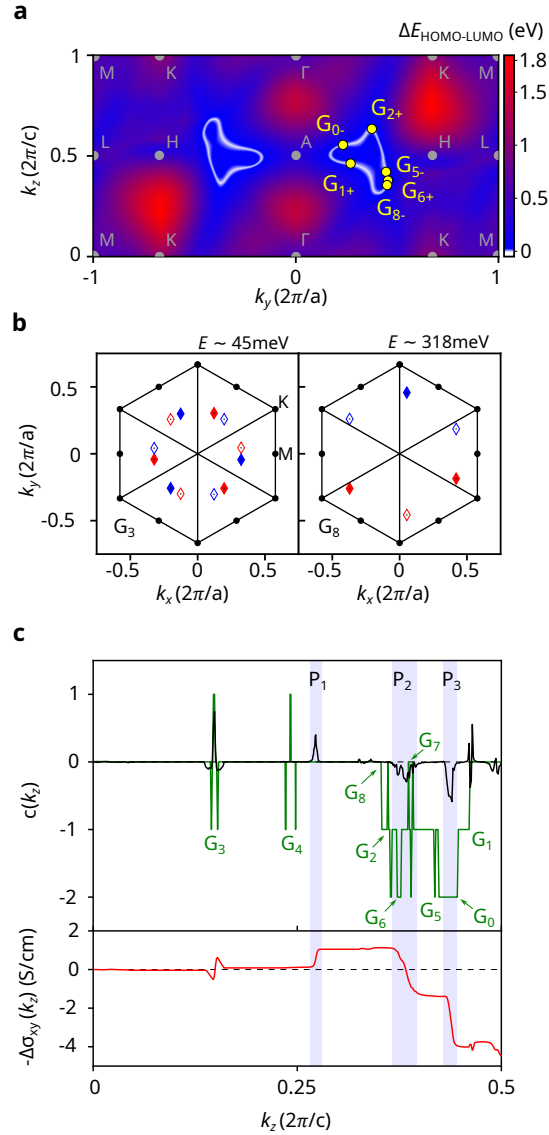


FIG. 3. **Nodal lines and the origin of the anomalous Planar Hall effect in PtBi₂.** **a:** Energy gap ΔE between HOMO and LUMO bands in the k_y, k_z (mirror) plane. The nodal loops ($\Delta E = 0$) appear in white. When $B \neq 0$, each nodal loop splits into 6 Weyl nodes (WN, yellow points), forming 6 groups of 6-WN. The signs denote the chiralities. **b:** Two groups of WN of HOMO-LUMO for a Zeeman energy $E_Z = 14 \text{ meV}$: G_3 is the 12-fold set of WNs closest to E_F already present at $B = 0$, and G_8 is one of the six 6-fold groups mentioned above. The average energies of the groups are shown. Red (blue) markers denotes positive (negative) chirality, while full (empty) markers denote the positive (negative) k_z position of the WN ($G_3 : k_z \sim \pm 0.149$, $G_8 : k_z \sim \pm 0.358$). Solid lines represent the mirror planes, while the dots show the high-symmetry points. **c:** (Top) Chern number $c(k_z)$ in an ideal (green, full HOMO) and a more realistic (black, $E_F = E_{G_3} = 45.3 \text{ meV}$) case, with a Zeeman energy $E_Z = 14 \text{ meV}$. In the ideal case, the Chern number jumps discretely by ± 1 at each WN, while the variation is smoothed out in the realistic case. (Bottom) Anomalous Hall conductivity $-\Delta\sigma_{xy}(k_z)$ calculated from the Chern signal in the realistic case (in black above). The 12 WNs from G_3 at low k_z contribute very little to the AHC, as the Berry curvature they generate is nearly compensated. Most of the AHC comes from 2 peaks in the Chern number at higher k_z , P_2 and P_3 (shown in blue). A third peak at lower k_z , P_1 , attenuates the total AHC amplitude, and is found to correspond to WNs from nodal lines below the HOMO band (see Supplementary materials sec. S11). Only the $k_z > 0$ dependences are shown, as $c(k_z)$ is even and $\Delta\sigma_{xy}$ is odd in k_z .

SUPPLEMENTARY MATERIALS

Methods

Sample Preparation

High-quality single crystals of PtBi_2 were grown using the self-flux method [26]. These crystals were mechanically exfoliated to obtain thin flakes, with widths exceeding $10\ \mu\text{m}$ and thickness ranging from a few dozen to a few hundred nanometers. The flakes were contacted with Cr/Au using standard e-beam lithography techniques. Prior to the metal deposition, a small Ar-etch was performed to eliminate any surface oxidation. The main sample used in this study is denoted as *D1* (70 nm thick), and supplementary information includes corroborating results for a second sample, *D2* (126 nm thick). In a previous study[24], the two dimensional superconductivity of these samples were studied in details at sub-Kelvin temperatures. Here, we focus on measurements performed above 1K, above the superconducting transition. No evidence of aging effects was observed between the two studies, as indicated by the absence of any measurable change in the residual resistance ratio ($RRR = R(300\text{K})/R(4\text{K})$).

Measurement Setup

The measurement configuration consists of a standard Hall-bar geometry. A current is injected between the source and the drain as depicted in Fig. 1.d. Longitudinal and transverse resistances (indicated in red and black, respectively) are measured along and across the sample relative to the current orientation.

Measurement set-up for samples D1 and D2.

Measurements were conducted in a Dynacool 14T PPMS using an insert equipped with a mechanical 2D rotator. By rotating the sample with the rotator, the angle φ between the fixed-axis magnetic field and the applied current can be adjusted over a full range of 360° (with φ the angle between the magnetic field and the electric field). The resistances were measured using external lock-in amplifiers, with an AC current of $100\ \mu\text{A}$ at a frequency of $927.7\ \text{Hz}$, with an integration time of 300 ms. At such low currents, no thermal effects are expected. For sample *D1*, for measurements taken at $T = 5\ \text{K}$ and $B = 1, 2, 3, 4, 5, 6, 7, 10\ \text{T}$, as well as at $B = 14\ \text{T}$ and $T = 5, 10, 20, 50, 300\ \text{K}$, 10 points were measured at each angular position, taking the averaged value of the resistance. The angular step for each measurement was 1° . All measurements on sample *D2* were conducted with the same parameters. For sample *D1*, more precise measurements were taken at $T = 5\ \text{K}$ and $B = 14\ \text{T}$, as well as at $B = 14\ \text{T}$ and $T = 100, 200\ \text{K}$, with an averaging over 40 measurement points at each angular position. The angular step for each measurement was

0.5° , and the results were interpolated with a step of 1° , to perform the analysis in the same way for each pair of (B,T) parameters.

At low temperature ($T \leq 20\text{K}$) the first oscillation of the APHE ($0^\circ \leq \varphi \leq 120^\circ$) is not fully visible even at 14T, although it is consistently observed for $T \geq 50\ \text{K}$ (see at $T = 100\text{K}$ in Fig. 2.a and Supplementary sec. S5 and sec. S4). This partial suppression of the signal likely stems from the mechanical rotator: When the stepper-motor at the top of the measurement stick turns by a small angle (in our measurements, the angular step is 1°), the mechanical rotator in the cryostat will move by an inconsistent angle (around the target step, e.g. 1°). As we measure the angle of the rotator at the top of the stick, and not the actual angle of the sample at the bottom, this creates small deviations of the PHE signal away from a π -periodic oscillation. When a π -periodic background is removed from the data (to evidence the APHE signal), these deviations are carried to the residues, and can corrupt the signal. These artifacts are reproducible, and decrease with temperature, as would be expected with mechanical rotator inconsistencies.

Measurement set-up for sample D3.

Measurements were conducted in a VTI equipped with a 3D-piezorotator and a large bore 14T magnet. In this work, we show in-plane rotation measurements. By rotating the sample with the rotator, the angle φ between the fixed-axis magnetic field and the applied current can be adjusted over a 180° range (with φ the angle between the magnetic field and the electric field). In order to have the full 360° range, we flip the orientation of the sample by 180° along the perpendicular axis. This is equivalent to reverse the direction of the magnetic field. The resistances were measured using external lock-in amplifiers, with an AC current of $500\ \mu\text{A}$ at a frequency of $331\ \text{Hz}$, with an integration time of 300 ms. For sample *D3*, for measurements taken at $T = 3, 20, 100\ \text{K}$ for fields ranging between 1 T and 14 T. Contrary to the measurement of *D1* and *D2*, a single point was measured at each angular position.

Planar Hall Effect

The contributions of the planar Hall effect/anomalous magnetoresistance to the longitudinal resistivity ρ_{xx} and transverse resistivity ρ_{yx} obey the following angular dependence [3, 13]:

$$\begin{aligned}\rho_{xx}^{\text{AMR}}(\varphi) &= \rho_{\perp} - \Delta\rho \cos^2 \varphi, \\ \rho_{yx}^{\text{PHE}}(\varphi) &= -\Delta\rho \cos \varphi \sin \varphi,\end{aligned}\tag{1}$$

with $\Delta\rho = \rho_{\parallel} - \rho_{\perp}$ the amplitude of both the PHE and the AMR; ρ_{\parallel} and ρ_{\perp} the resistivities when \mathbf{B} is respectively along and perpendicular to the electrical field (current); and φ the angle between the magnetic and electric fields (i.e. current lines) in the sample. The PHE signal is therefore characterized by π -periodic oscillations for

both ρ_{xx} and ρ_{yx} (when rotating the magnetic field in the sample's plane, with a fixed current) with the same amplitude, with a $\pi/4$ offset between the two. The maxima of ρ_{xx} correspond experimentally to the orientation of the current in the sample.

Computation details

We performed a full-relativistic non-magnetic calculation using the full potential local orbital (FPLO) code [27] version 22.01 within the generalized gradient approximation (GGA) [28]. From the DFT result a 72-band

Wannier function (WF) model was extracted consisting of Bi6p and Pt6s5d type WFs. A constant magnetic field Zeeman term $H^{\text{Zeeman}} = \mathbf{B}\mu_B \langle \mathbf{S} \rangle$ was added to the model using the WF representation of the spin operators $\langle \mathbf{S} \rangle$.

The anomalous planar Hall signal $\Delta\sigma_{yx}$ can be computed by calculating the Chern signal $c(k_z) = \frac{1}{2\pi} \int F_z(\mathbf{k}) d\mathbf{S}$ for a number of k_z -planes with subsequent integration over k_z . For an assumed constant homo $c(k_z)$ can be obtained by a plaquette type integration (see sec. S10 and Ref. [29]) and with a Fermi level by a simple Riemann-sum integral.

Materials

S1. Resistivity in the anomalous planar Hall effect

It is expected from the theory [6] that the conductivity generated by the anomalous planar Hall effect (APHE) follows the angular dependence

$$\begin{aligned}\sigma_{xx}^{\text{APHE}}(\varphi) &= 0, \\ \sigma_{yx}^{\text{APHE}}(\varphi) &= \Delta\sigma_{yx} \cos 3\varphi.\end{aligned}\tag{S2}$$

In order to obtain the angular dependence of the resistivity associated with the APHE, we assume an underlying constant (Drude) longitudinal conductivity $\sigma_{xx} = \sigma_D$, so that the overall conductivity matrix becomes $\sigma = \begin{pmatrix} \sigma_D & \sigma_{xy} \\ -\sigma_{xy} & \sigma_D \end{pmatrix}$, with $\sigma_{xy} = \sigma_{xy}^{\text{APHE}}(\varphi)$ from eq. S1. By inverting the conductivity matrix, we obtain the resistivity matrix $\rho = \sigma^{-1} = \begin{pmatrix} \rho_{xx} & \rho_{xy} \\ -\rho_{xy} & \rho_{xx} \end{pmatrix}$, with

$$\begin{aligned}\rho_{xx} &= \frac{\sigma_D}{\sigma_D^2 + \sigma_{xy}^2} = \frac{1}{\sigma_D(1 + (\sigma_{xy}/\sigma_D)^2)}, \\ \rho_{xy} &= -\frac{\sigma_{xy}}{\sigma_D^2 + \sigma_{xy}^2} = \frac{\sigma_{xy}/\sigma_D}{\sigma_D(1 + (\sigma_{xy}/\sigma_D)^2)}.\end{aligned}\tag{S3}$$

Here, we can see that the APHE has a more complicated effect on the resistivity than on the conductivity, with both ρ_{xx} and ρ_{xy} having $2\pi/3$ -periodic components in φ . The shape of the oscillation depends strongly on the relative amplitude $r = \Delta\sigma_{xy}/\sigma_D$ of the AHC oscillation with respect to the longitudinal conductivity (see Fig. S1.A,B,C). For $r \ll 1$, both ρ_{xx} and ρ_{xy} tend towards sine waves of period $\pi/3$ and $2\pi/3$, respectively. The amplitudes of the oscillations of ρ_{xx} and ρ_{xy} (defined as $\Delta\rho = [\max(\rho) - \min(\rho)]/2$) depend on the ratio r as r^3 and r^2 , respectively, meaning that for $r \ll 1$, the oscillations in ρ_{xx} will be much lower than those in ρ_{xy} (see Fig. S1.F).

As the ratio r is proportional to the angular mean value $\bar{\rho}_{xx}$ of ρ_{xx} , this means that for a given amplitude of the oscillations in AHC, the APHE in resistivities will deviate from sine waves when the longitudinal resistivity is too high, and the oscillations will vanish if the longitudinal resistivity is too low. For our sample, we can roughly estimate a ratio $r = \frac{\Delta\sigma_{xy}}{\sigma_D} \sim 2.7 \times 10^{-3}$, by taking $\sigma_D = 1/\bar{\rho}_{xx} = 1/(R_{xx}(B=0)/N_{\square}) \sim 1/(0.8/0.3)$ and $\Delta\sigma_{xy} = 0.001$, which gives an amplitude of the oscillations of ρ_{xy} of about $7\mu\Omega$, close to what we see at 14T (see Fig. 2.d). At this value, the oscillations in ρ_{xy} are very close to a sine wave, and the oscillations in ρ_{xx} are about 3 orders of magnitude smaller. This shows that, in our case, we can simply treat the signature of the APHE in resistivity as

$$\begin{aligned}\rho_{xx}^{\text{APHE}}(\varphi) &= 0, \\ \rho_{xy}^{\text{APHE}}(\varphi) &= A^{\text{APHE}} \cos 3\varphi.\end{aligned}\tag{S4}$$

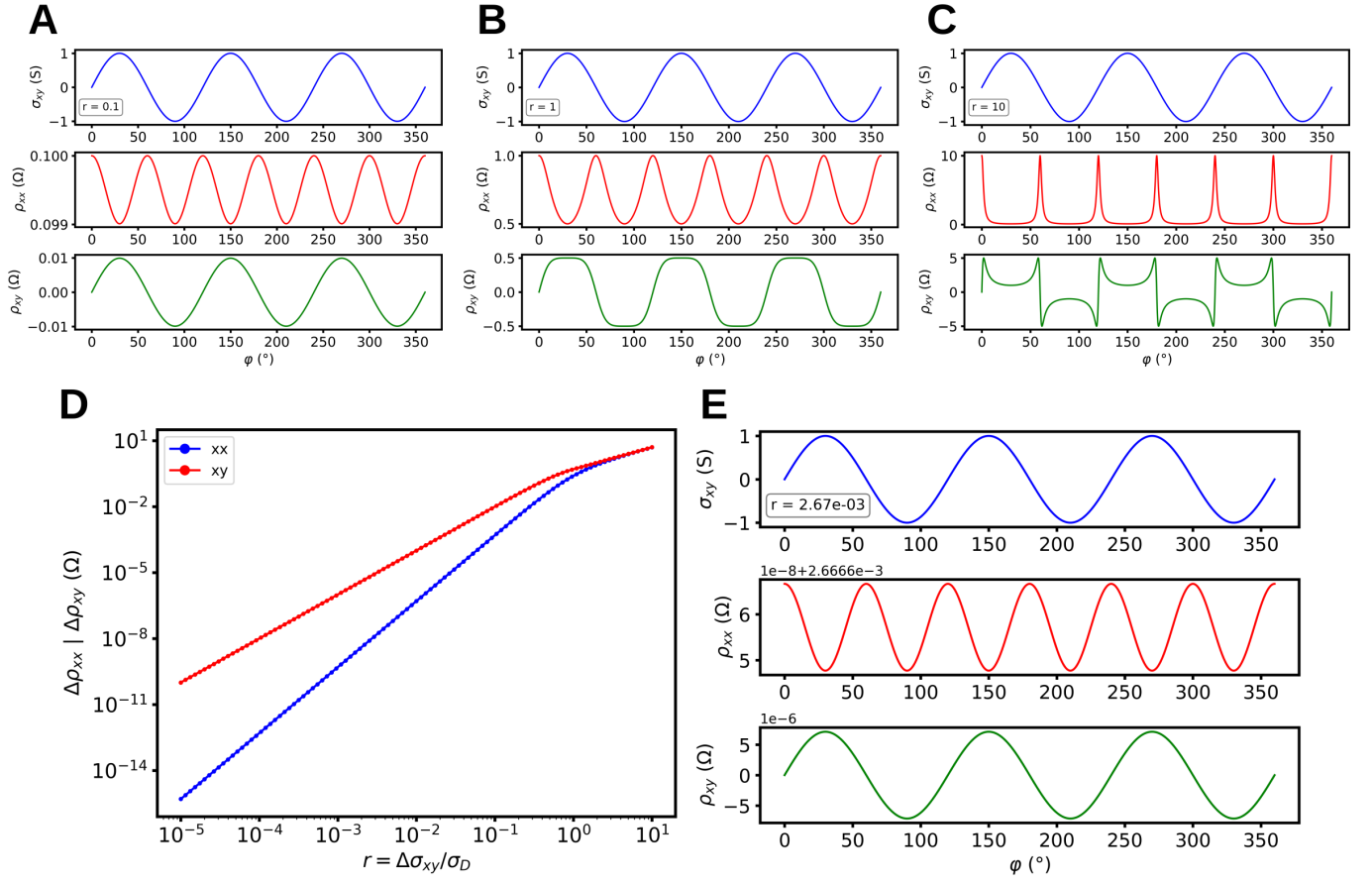


Figure S1. Resistivities of the APHE. a,b,c: ρ_{xx} and ρ_{xy} obtained from σ for the ratios 0.1,1 and 10. d: Amplitude of the oscillations of ρ_{xx} and ρ_{xy} with respect to the ratio r , in log scale. e: ρ_{xx} and ρ_{xy} obtained for a realistic value of $r = 2.67 \times 10^{-3}$.

S2. Residues extraction for APHE vs B

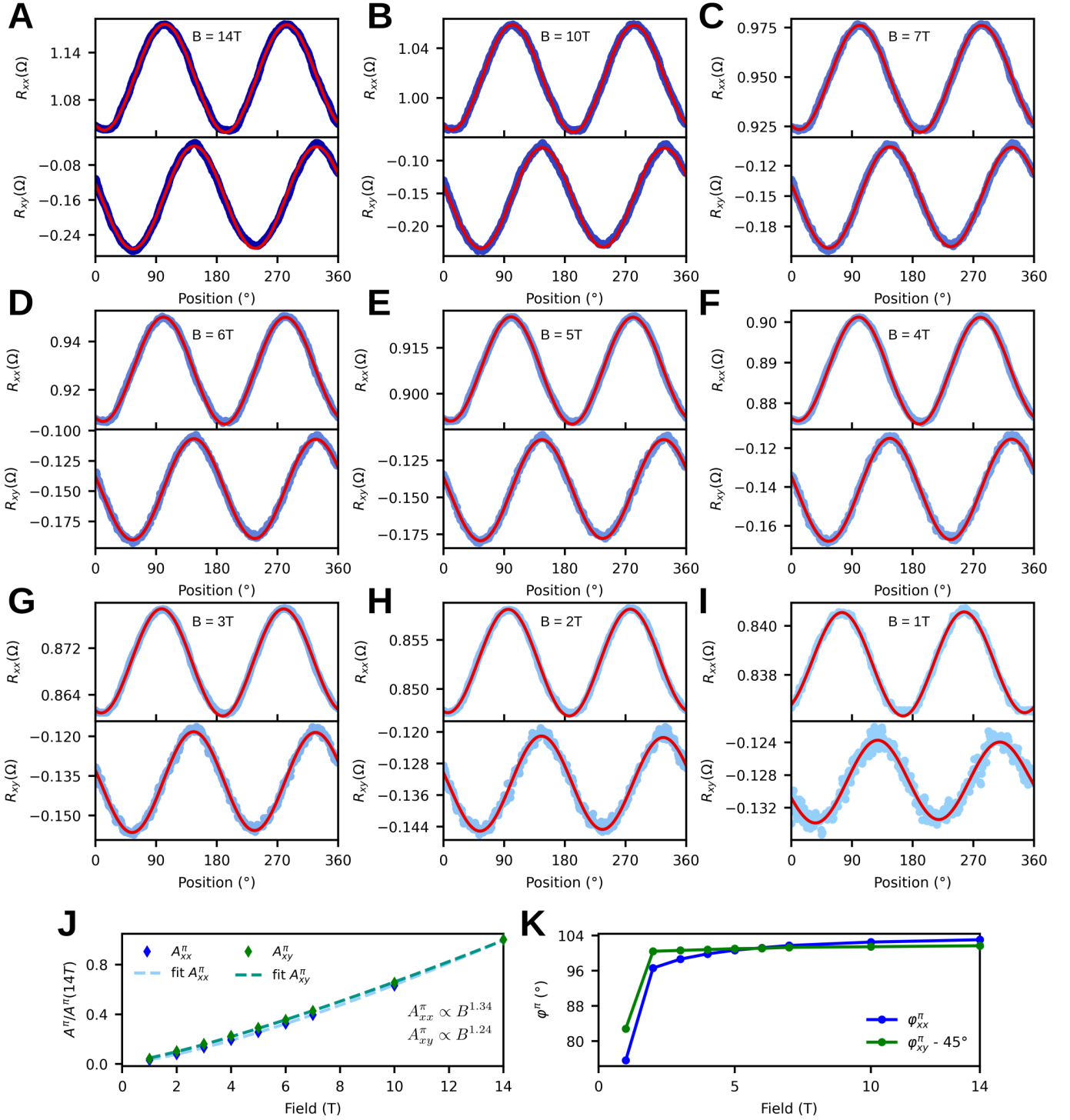


Figure S2.

In order to extract as much of the background and PHE as possible, and try to keep only the APHE, we can fit R_{xx} and R_{yx} separately at each field with a simple model:

$$\bar{R}(\varphi) = C + A^{2\pi} \cdot \cos(\varphi - \varphi_{2\pi}) + A^{\pi} \cdot \cos[2(\varphi - \varphi_{\pi})], \quad (\text{S5})$$

with C an angle-independent constant, and A^π and $A^{2\pi}$ the amplitudes of some π - and 2π -periodic signals, with angular origins φ_π and $\varphi_{2\pi}$, respectively. The π -periodic component should remove the PHE signal from the measurements, while the angle-independent and 2π -periodic components should remove the magnetoresistance signal from the perpendicular field component (respectively for the misalignment between the rotation plane and magnetic field axis, and for the misalignment of the sample's plane with the rotation plane). All the above parameters are independent between R_{xx} and R_{yx} , and are assumed to be field- or temperature-dependent. Fits of the data at each magnetic field are shown in red in Fig. S2.A-I. The residues ΔR are then obtained by subtracting the previous fit from the data: $\Delta R = R - \bar{R}$.

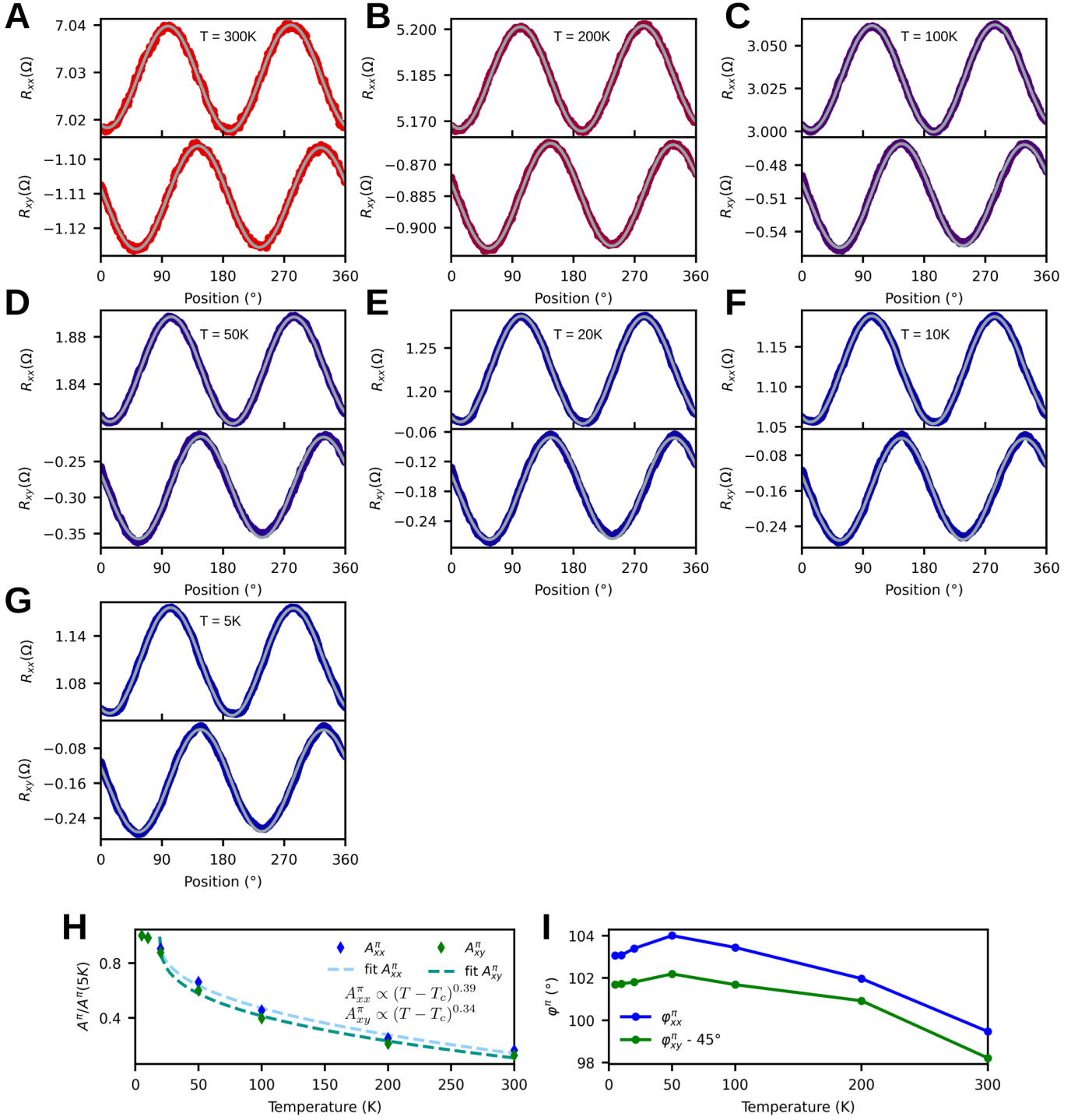
S3. Residues extraction for APHE vs T 

Figure S3.

We perform the exact same analysis as in sec. S2 at 14T and multiple temperatures, from 5K to 300K. The fits are shown in grey in Fig. S3.A-G.

S4. APHE vs B

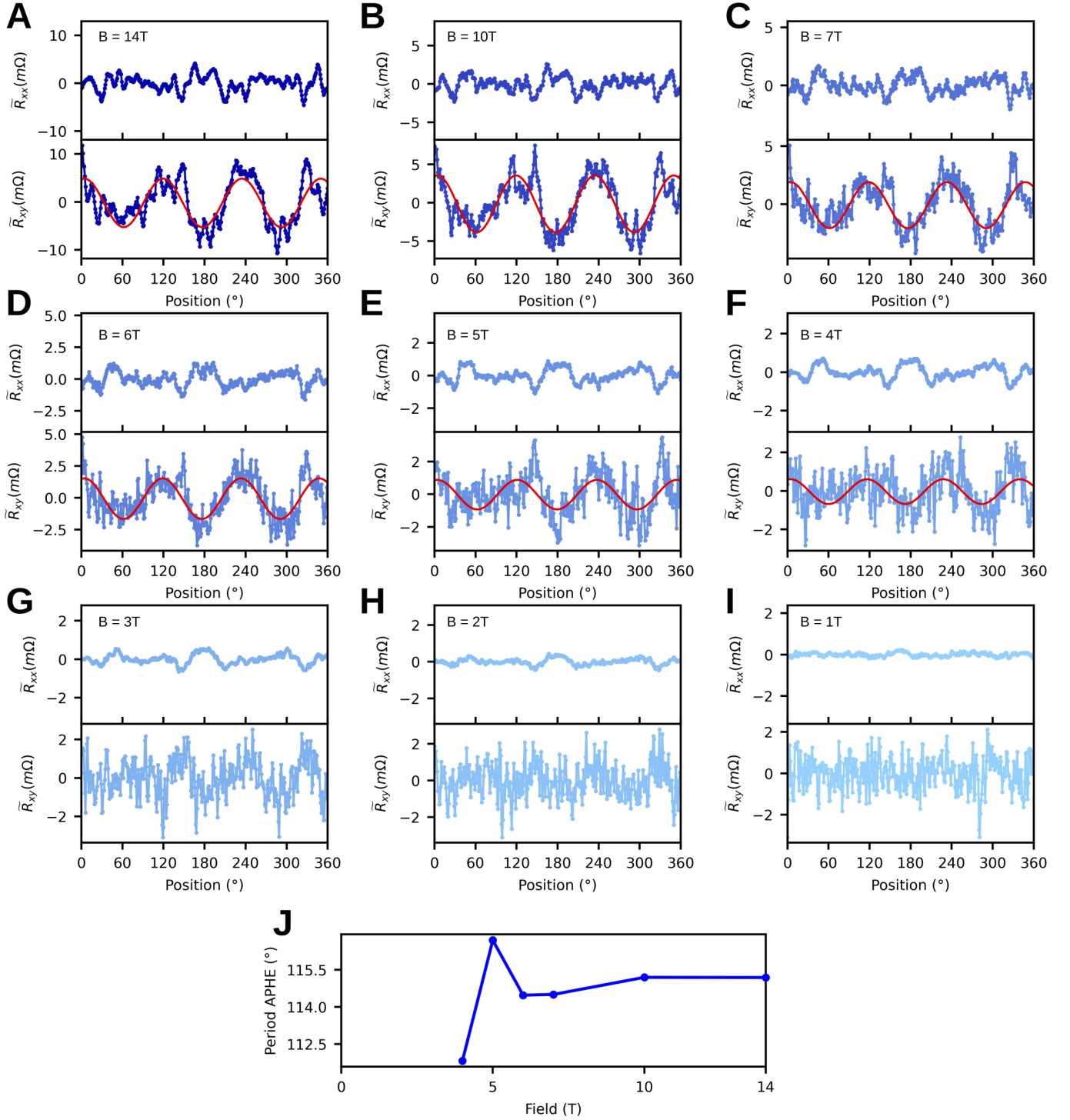


Figure S4.

Fig. S4.A-I shows the longitudinal and transverse residues $\Delta R = R - \bar{R}$ obtained in sec. S2 at 5K for each magnetic field from 1T to 14T. For $B \geq 4$ T, a roughly $2\pi/3$ -periodic signal emerges in ΔR_{yx} , which corresponds to the APHE. We fit this signal with the following formula:

$$\Delta R_{yx}(B, \varphi) = C(B) + A^{\text{APHE}}(B) \cos[(\varphi - \varphi_0) \cdot 2\pi/P^{\text{APHE}}(B)], \quad (\text{S6})$$

with C a field dependent offset ; A^{APHE} the amplitude of the APHE ; φ_0 the field-independent angular origin of the oscillation ; and P^{APHE} the angular period of the APHE, which is considered field-dependent in the analysis. The fits obtained above 4T are shown in red in Fig. S4.A-I, and fit the data very well between $120^\circ \leq \tilde{\varphi} \leq 360^\circ$. The residues deviate slightly from the fit below 120° , most probably due to non-uniform movement of the mechanical rotator in this angular range at low temperature. This issue is much more visible in a second sample, D2 (126nm thick, see e.g. Fig. S6.A,B), and happens around specific positions in a reproducible manner. This low-angle deviation disappears at higher temperature (see sec. S5), which also points towards a low-temperature mechanical issue of the rotator. Fig. S4.J shows the field dependence of P^{APHE} yielded by the fit. Above 6T, it is stable at $P^{\text{APHE}} \sim 115^\circ$, or just under the 120° expected for the PHE from theory. The low-field variation of the period could be the result of lower signal/noise ratio combined with the mechanical rotation issues. The variation of A^{APHE} with field is shown in the main text in Fig. 2.g.

S5. APHE vs T

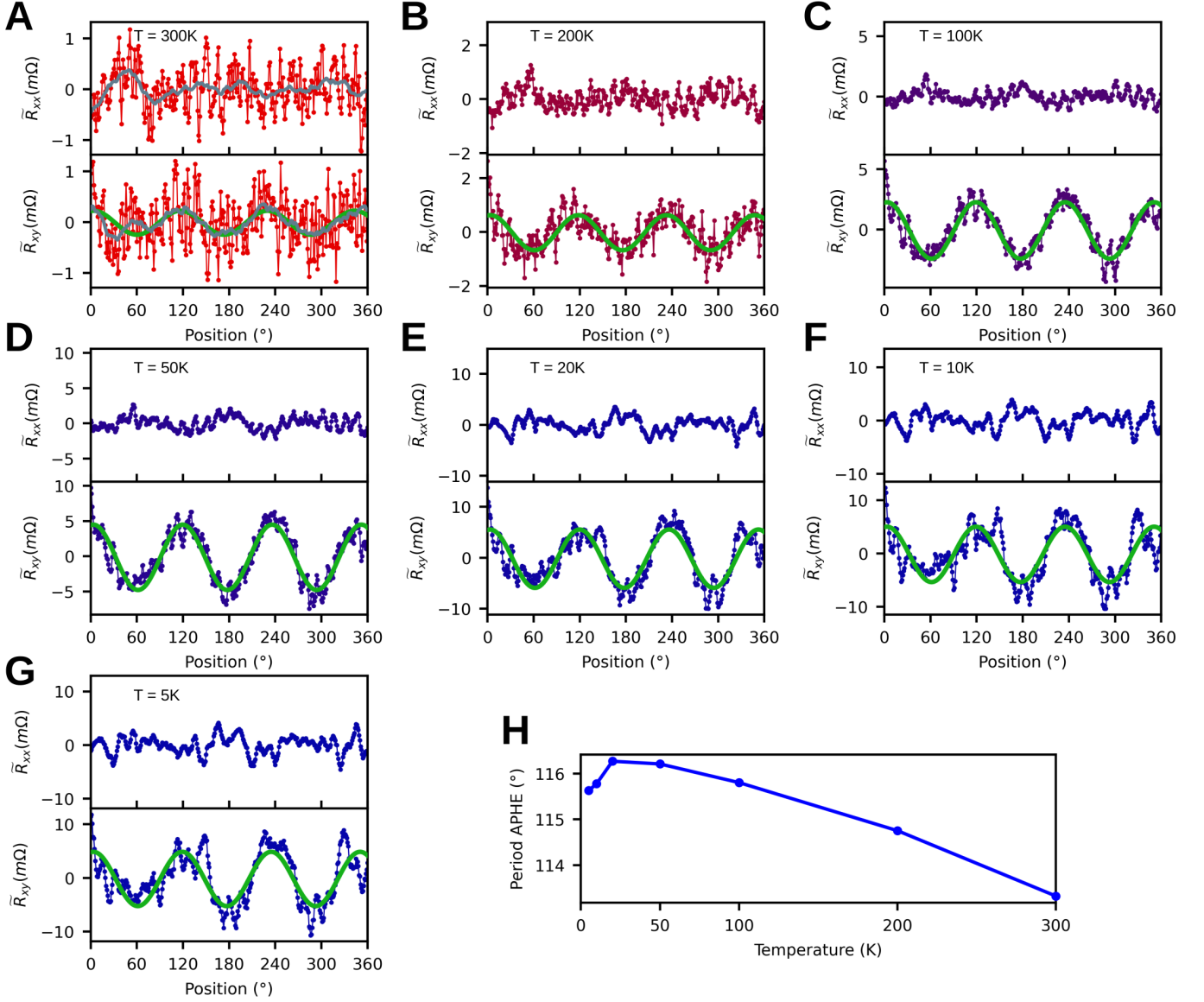


Figure S5.

Fig. S5.A-G shows the longitudinal and transverse residues $\Delta R = R - \bar{R}$ obtained in sec. S3 at 14T for each temperature from 5K to 300K (same data as in Fig. 2.d-f, main text). The raw residues are fitted with eq. S6, with the temperature as a parameter instead of the field, and the resulting fits are shown in green. The low-angle deviation from the fit observed in sec. S4 persist until $T \sim 50$ K, above which they are no longer visible, and the fit follows the data closely over the entire angular range.

As the temperature is increased, the amplitude of the APHE decreases (see Fig. 2.h, main text). At 300K (Fig. S5.A), the APHE is no longer visible to the naked eye because of the low signal/noise ratio. However, by applying a simple Savitzky-Golay smooth (in grey), the $2\pi/3$ -periodic oscillation becomes clearly visible, and follows closely the fit of the raw data (in green). Applying the same smooth to the longitudinal residuals does not yield any similar trend.

The Savitzky-Golay smooths were done with the `savgol_filter` function from the `scipy.signal` library in Python, with 31° of window size and a polynome order of 1. The boundary conditions were set to 'wrap' (i.e. periodic) for the transverse residues, and 'nearest' for the longitudinal residues.

S6. PHE and APHE at 126nm

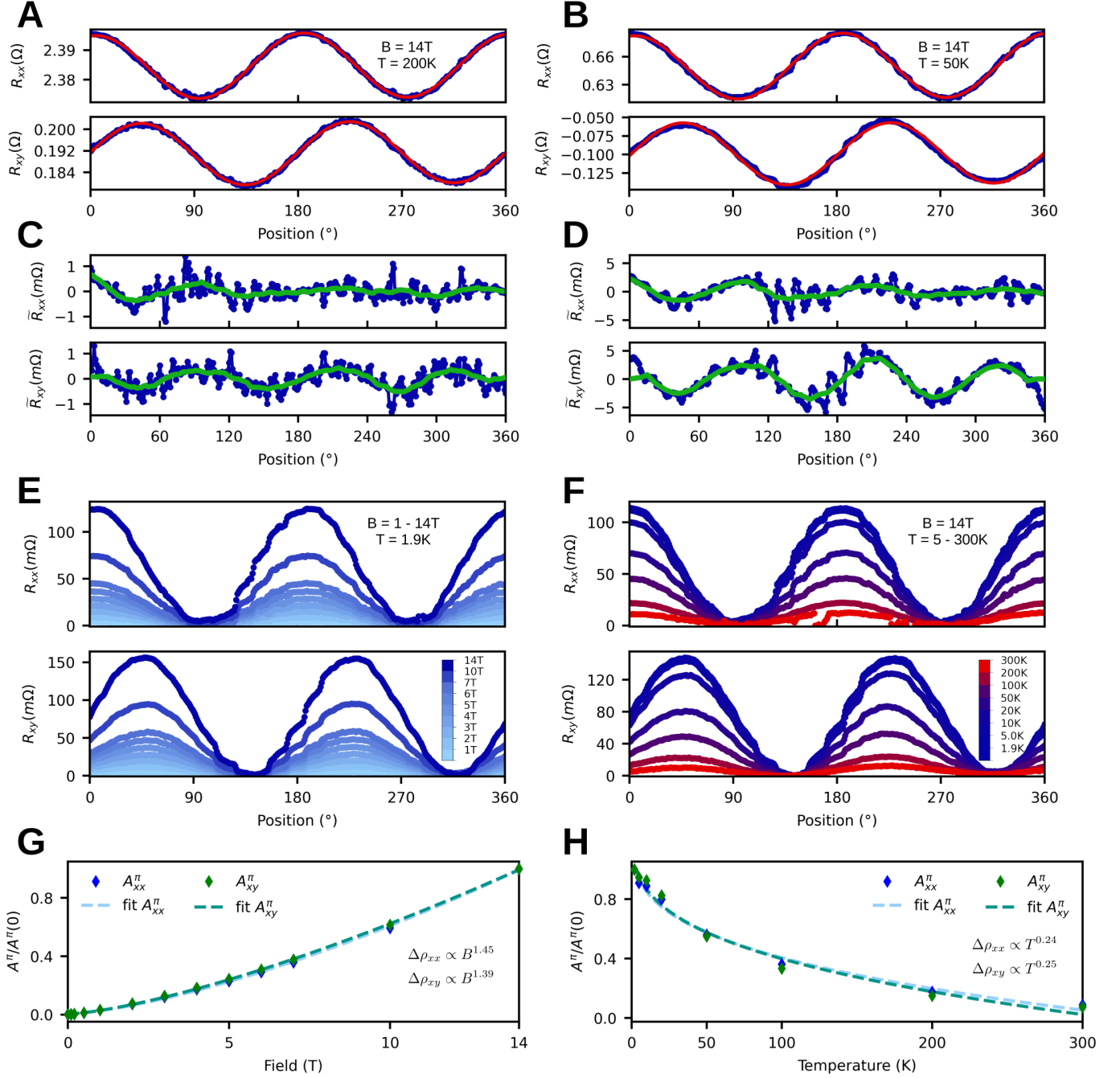


Figure S6.

Similar measurements and analysis as for sample *D1* were performed on another sample, *D2* (126nm thick). However, this sample proved more sensitive to the issues of the mechanical rotator than *D1*, and the APHE signal was not necessarily visible in all residues extracted, due to increased noise levels.

Fig. S6 shows the main results for sample *D2*. Fig. S6.A,C show the resistance and residues at 200K, 14T. The resistance is fitted with eq. S5 (red), and the residues are smoothed with the same procedure as described in sec. S5 (green). Fig. S6.B,D show the same data, but at 50K, 14T. At both temperatures, the data residues show a clear oscillation corresponding to the APHE.

S7. PHE and APHE at 320nm

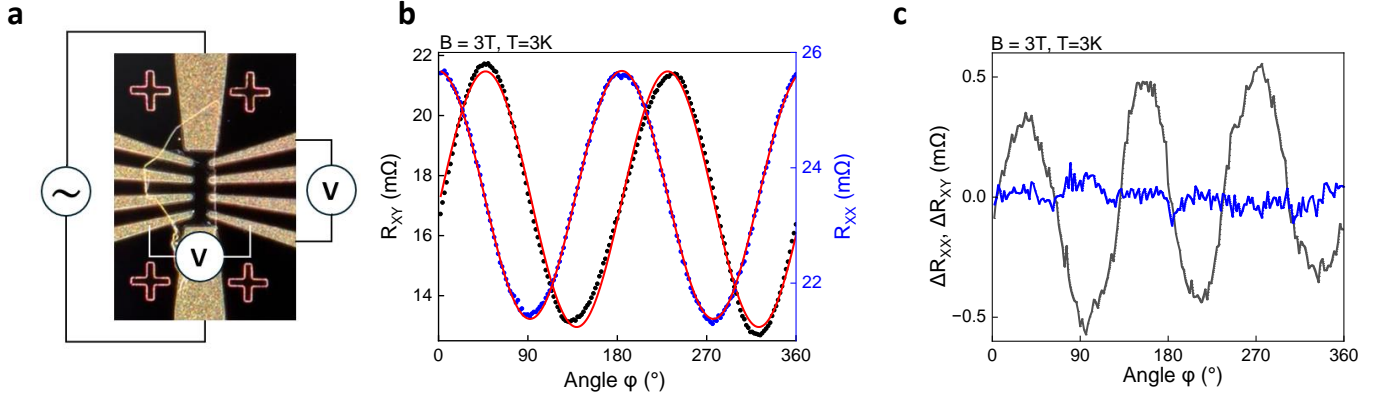


Figure S7. **a:** Optical image of the device and schematic diagram of the measurement configurations. The Hall bar is $50\mu\text{m}$ long and $10\mu\text{m}$ large. **b:** Angular dependence of R_{yx} (black) and R_{xx} (blue) at $B = 3$ T, and $T = 3$ K. The best fits with 1 (Methods) are superimposed in red. **c:** Angular dependence of the residues ΔR_{yx} (grey) and ΔR_{yx} (blue) after a background removal. Only a π -periodic signal was removed for the present analysis and a 2π -periodic signal is therefore still visible in the residues of ΔR_{yx} .

We have also exfoliated and measured a 320nm thick PtBi_2 flake (sample D3, see fig. S7 a). The flake was contacted by optical lithography and for such thick flake, the residual resistance ratio is much larger than for D1 or D2 : $RRR = 25$.

As already stated in the methods, the flake was measured in a different set-up and using a 3D-piezorotator. The analysis was done following equation 1 in the Methods, and only a π -periodic signal was removed from the longitudinal and transverse resistances (fig. S7 b). As a result, an additional weak 2π signal can be seen in the residual of the transverse resistance. As a confirmation of the results obtained for D1 and D2, a very clear $2\pi/3$ -periodic signal can be seen in the transverse resistance whereas no $2\pi/3$ -periodic oscillation could be identified in the longitudinal resistance (fig. S7 c).

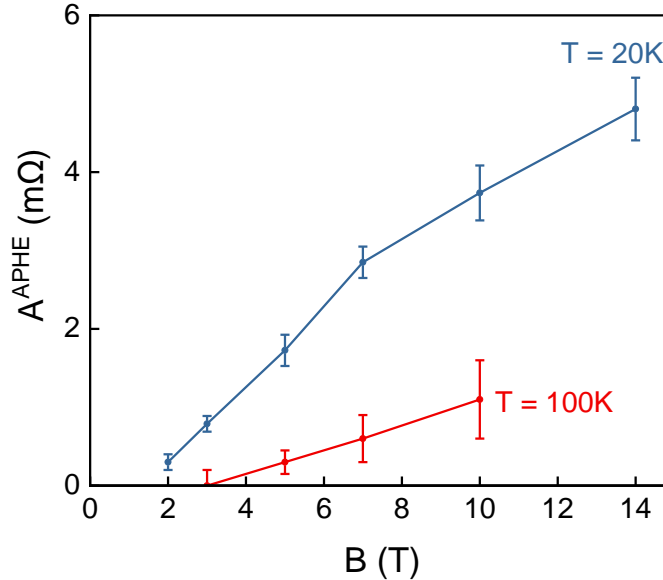


Figure S8. Amplitude of the APHE signal as a function of the magnetic field and for $T = 20$ K (blue) and $T = 100$ K.

For D3, the evolution of the APHE signal was measured as a function of the magnetic field for two temperatures : $T = 20$ K and $T = 100$ K (fig. S8). A clear temperature dependence of the field onset could be evidenced, with a higher onset seen at higher temperature, supporting our hypothesis that the field onset is linked to the effective gap

of the TNLs.

S8. Residual Resistance Ratio

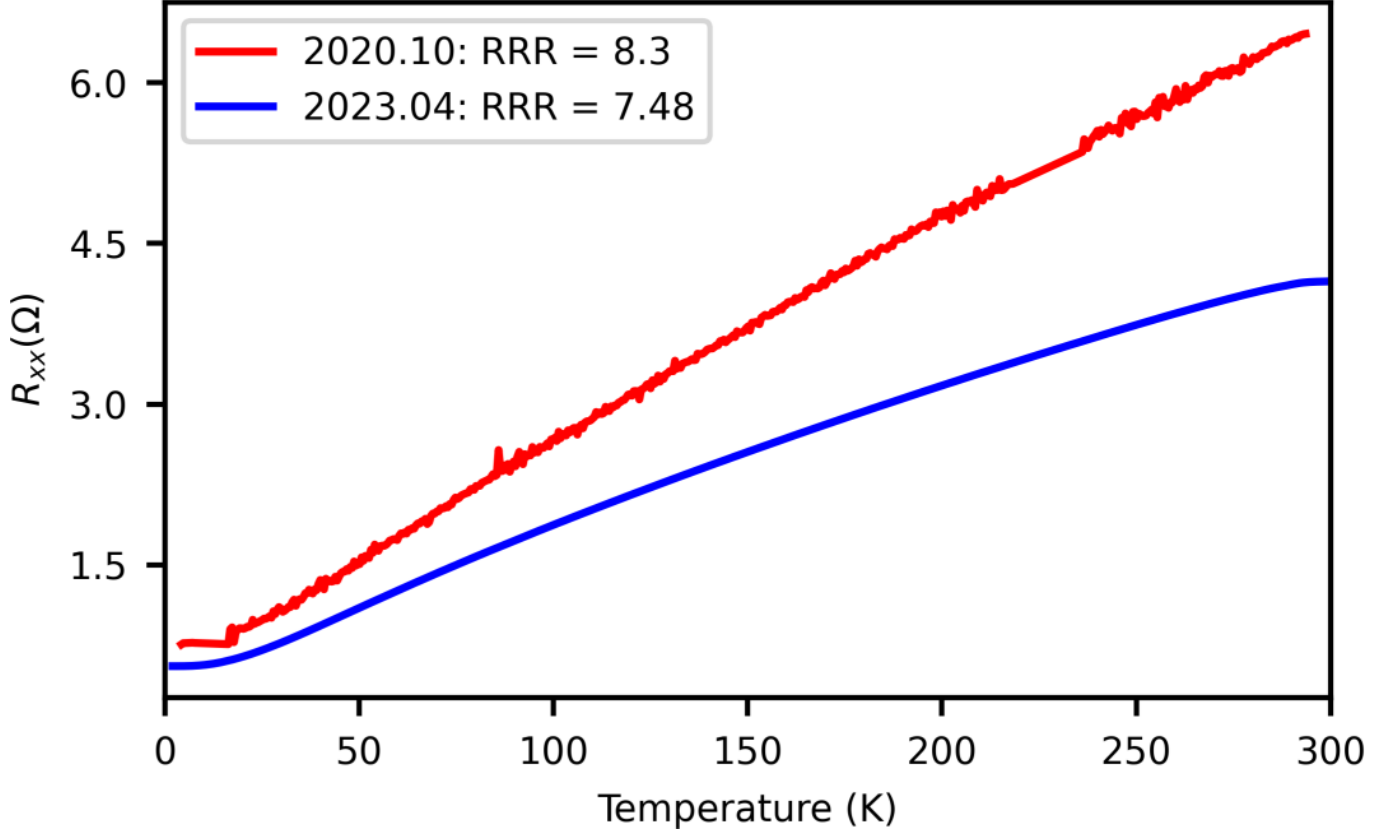


Figure S9.

Fig. S9 shows a comparison of the longitudinal resistance of sample *D1* between two cooldowns from room temperature to 5K, in 2020 (red, see Ref.[24]) and in 2023 (blue, this measurement run). The residual resistance ratio $RRR = \frac{R(300K)}{R(5K)}$ is similar between the two cooldowns, and only decreased slightly in 2.5 years, showing the stability of the samples in air.

S9. The Weyl point geometry of band 48

We focus on the band number 48, which when being the highest fully occupied band yields the correct number of electrons of the system. Of course the compound is not an insulator, however the Weyl points reported before are formed by band 48 and 49 and in the region $k_z \lesssim 0.17 \frac{2\pi}{c}$ the highest occupied band is band 48.

As it turns out band 48 has more than the previously reported Weyl points. We group the Weyl points (WP) according to their averaged energy. We get six groups of six and three groups of twelve WPs with the exception of group G_8^{48} , see below. Within each group the WPs have individual $k_{x,y,z}$ coordinates of which the k_z positions are clustered very closely around $\pm |k_{z0}|$ with a group specific $|k_{z0}|$. The only (always fulfilled) true symmetry is ΘM_x . However, the deviations from the non-magnetic symmetries are small, such that the twelve-fold groups approximately follow $\{E, \Theta\} C_{3v}$, while the six-fold groups follow this symmetry if the WPs are assumed to lie exactly on the mirror planes. Group G_8^{48} is an exception in that it shows cross-over behavior between a 12-fold and a six-fold case as a function of increasing magnetic field. From the symmetry and from the small displacements shown in Fig. S10, Fig. S11 and Fig. S12 it is clear that the twelve-fold groups survive the transition to $B = 0$, while the six-fold groups must dissolve in the nodal loops on the mirror planes.

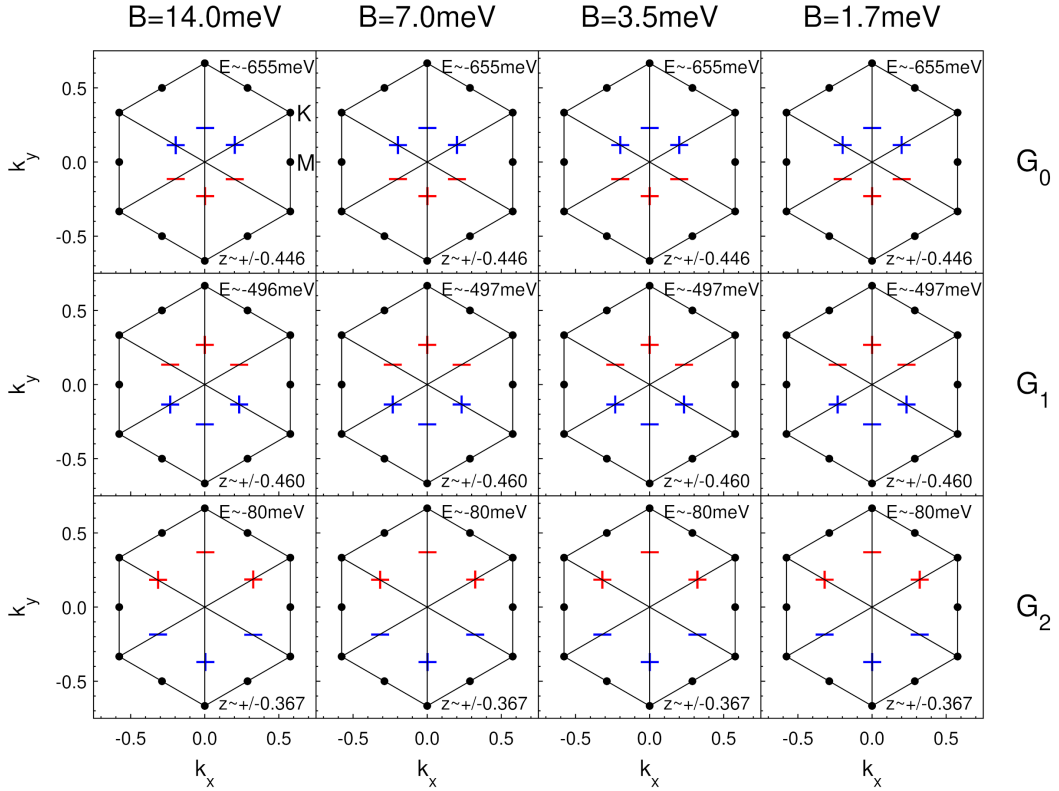


Figure S10. WP groups 0, 1 and 2 of band 48. The average energy and k_z -position is denoted. Plus/minus signs denote the sign of the k_z -position and red/blue mark positive/negative chirality, resp.

The cross-over behavior of group 8 demonstrates both the survival of the twelve-fold groups as well as the dissolution of the six-fold groups. In Fig. S13 we follow the evolution of the three WPs close to the positive y -axis of Group G_8^{48} (Fig. S12 lower right panel). For high field ($B = 14 \text{ meV}$) we have a six-fold group (in this case shifted to the positive k_x -side of the mirror). At around $B = 3.5 \text{ meV}$ a WP dipole emerges on the negative k_x -side of the mirror, whose separation increases with decreasing field (Fig. S13). Approaching $B = 0$ the dipole part with equal chirality as the single WP from the six-fold subgroup is dissolved into the nodal loop, while the dipole part with opposite chirality to the single WP approaches the mirror symmetric position of the single six-fold WP, forming a fully symmetric twelve-fold group for $B = 0$. Apparently the emergence of the WP dipoles happens at different fields for the six points of the high-field six-fold group (last row of Fig. S12) as allowed by the magnetic symmetry. We want to stress that there is no symmetry which would force the appearance of six-fold or twelve-fold groups as already indicated by the

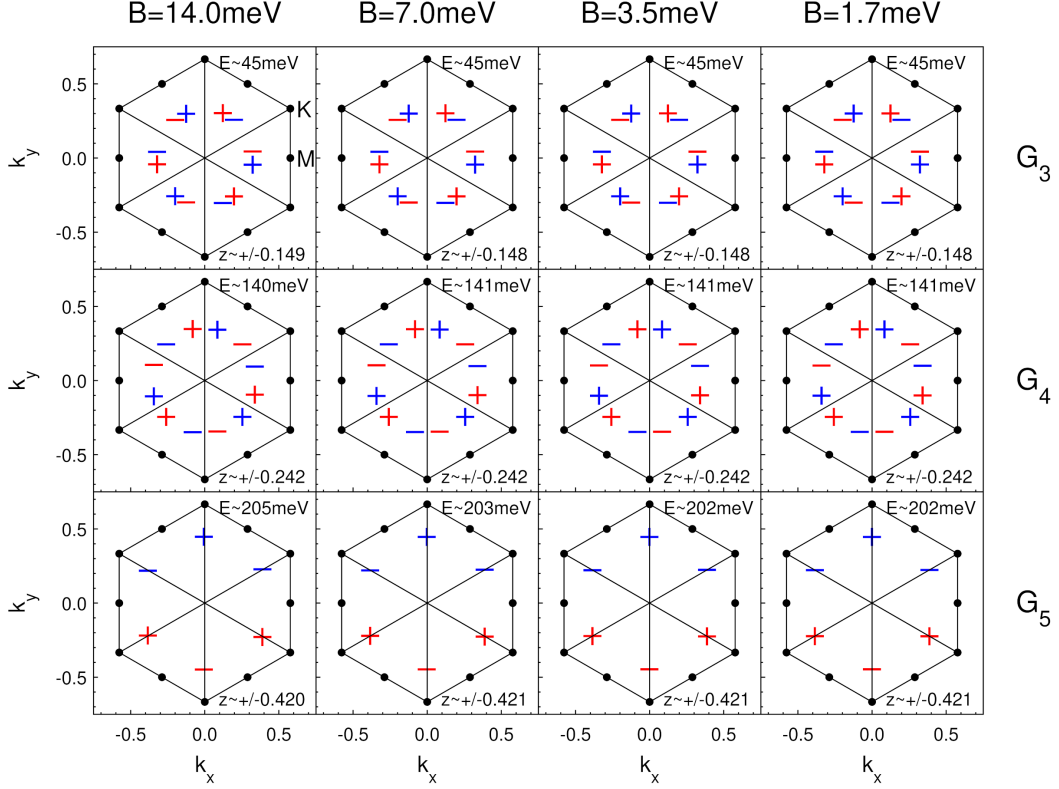


Figure S11. WP groups 3, 4 and 5 of band 48. Group 3 is the one close to the Fermi level. The average energy and k_z -position is denoted. Plus/minus signs denote the sign of the k_z -position and red/blue mark positive/negative chirality, resp.

behaviour of G_8^{48} . A group could have any even number of points as long as they occur in pairs as imposed by the magnetic symmetry.

It turns out that all but groups $G_{3,4}^{48}$ consist of at least some type II Weyl points, while these two groups are formed only by type I points.

S10. Chern signal

The Chern number of a k_z -plane is defined as

$$c(k_z) = \frac{1}{2\pi} \int dk_x dk_y F_z(\mathbf{k}) \quad (S7)$$

with $\mathbf{A}(\mathbf{k}) = \sum_n \langle u_n | i\nabla_{\mathbf{k}} u_n \rangle$, $\mathbf{F}(\mathbf{k}) = \nabla_{\mathbf{k}} \times \mathbf{A}(\mathbf{k})$, while the total anomalous Hall conductivity (AHC) is defined as

$$\begin{aligned} \Delta\sigma_{xy} &= -\frac{e^2}{\hbar} \frac{1}{(2\pi)^3} \int d^3k F_z(\mathbf{k}) \\ &= -\frac{e^2}{\hbar} \frac{1}{(2\pi)^2} \int dk_z c(k_z) \\ &= -\frac{e^2}{\hbar} \frac{1}{c2\pi} \int_0^1 dz c(z) \end{aligned}$$

with $c = 6.162\text{\AA}$ and conversion constant

$$\frac{e^2}{\hbar} \frac{1}{c2\pi} = 628.71\text{S/cm} \quad (S8)$$

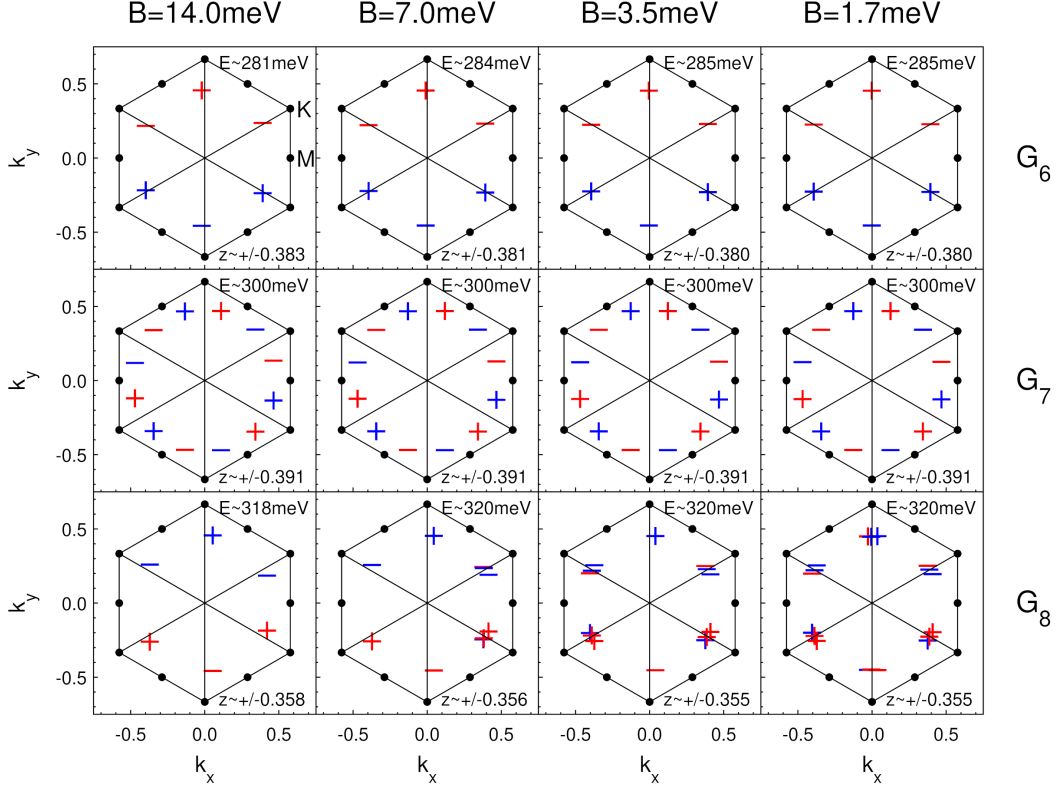


Figure S12. WP groups 6, 7 and 8 of band 48. The average energy and k_z -position is denoted. Plus/minus signs denote the sign of the k_z -position and red/blue mark positive/negative chirality, resp.

The Chern signal $c(k_z)$ can be obtained by a gauge invariant plaquette type integral [29], which has better convergence properties than a simple sum-type integral, but is only valid for a constant number of occupied bands, i.e. an insulating k_x, k_y -plane. $c(k_z)$ is given by the sum of $\tilde{c} = \frac{1}{2\pi} i \ln U_1 U_2 U_3 U_4$ over all plaquettes of the planar Brillouin zone perpendicular to k_z with $U_i = \frac{\det\langle u_{k_i} | u_{k_{i+1}} \rangle}{|\det\langle u_{k_i} | u_{k_{i+1}} \rangle|}$, where k_i are the k -points at the four plaquette corners. The determinant is taken of the overlap matrix formed by the 48 (homo) lowest bands. The minimally needed mesh fineness is dictated by the WP separation in the k_x, k_y plane and the mesh fineness of the k_z -interval by the k_z -separation of the individual WPs, which turns out to be demanding. Additionally, the experimentally used magnetic fields (\mathbf{B}) are small from a band structure perspective and the subsequent WP shifts (and emergence of new WPs) leads to strong variations of \mathbf{F} over rather small volumes.

To incorporate a Fermi energy eq. S7 is evaluated via a simple Riemann sum.

The Chern signal for the insulating case is entirely determined by the Weyl positions and hence the numerical results can be checked analytically. Each WP contributes a jump

$$c_{\text{WP}}(k_z) = \chi_{\text{WP}} \Theta(k_z - k_{z,\text{WP}})$$

The integral over k_z gives the contribution $\Delta\sigma_{xy,\text{WP}}(k_z) \propto -\chi_{\text{WP}}(k_z - k_{z,\text{WP}}) \Theta(k_z - k_{z,\text{WP}})$. The sum over all Weyl points for large k_z (total signal) then is

$$\Delta\sigma_{xy} \propto \sum_{\text{WP}} \chi_{\text{WP}} k_{z,\text{WP}} \quad (\text{S9})$$

For a subgroup of six WPs with vanishing total chirality around some positive k_z (half of a twelve-fold group) $\Delta\sigma_{xy}$ becomes a function of the k_z -separation of the individual WPs. It turns out that the WPs are ordered in three pairs of two points with opposite χ . Hence, each pair contributes an up-down jump combination (Fig. S14.C) with $\Delta\sigma = \chi \Delta k_z$ which is proportional to the separation of the points in the pair (up to some global integer, which is

determined by the numerical integrals). The separations Δk_z are small and in leading order a linear function of the field B (Fig. S14.A). Additionally, for group G_3^{48} , the separations Δk_z together with their χ compensate the linear field dependence of Δk_z completely, which results in very tiny total $\Delta\sigma_{xy}$ values, which depend quadratic on B (Fig. S14.B).

The χ -uncompensated three WP subgroups at positive k_z of a six-fold group give an effective jump $\Delta c = \pm 1$ at the group's averaged k_z -position. Since, the k_z positions of the groups can have sizable distances these well separated jumps contribute large values to $\Delta\sigma_{xy}$, in fact much larger than the actual result including the Fermi surface (black line) in Fig. 3 of the main text and Fig. S16 (keep in mind the conversion factor eq. S8).

The total result for $c(k_z)$ for four different fields B is shown in Fig. S15. Clearly the twelve-fold groups $G_{3,4,7}^{48}$ have compensating jumps within themselves and the separation of the individual jumps within such a group diminishes with diminishing field (Fig. S14.A). Each of these groups contributes a signal similar to the green line in Fig. S14.C. In contrast, the six-fold groups contribute effective jumps $\Delta c = \pm 1$ at different k_z positions each consisting of three closely spaced up-down-up or down-up-down jumps, whose internal separation diminishes with B , effectively becoming a single jump. Since the k_z positions of the group do not move around much with field, different groups do not compensate each other for $B \rightarrow 0$. The corresponding signal comes into existence immediately when $B > 0$, where these groups emerge out of the nodal loops. This situation is reminiscent of a quantum hall situation.

The discussion up to now was for a hypothetical insulating case where all bands up to the homo (48) are considered occupied. This means that all WPs of all groups are occupied exactly up to the touching point of the linear dispersion. This leads to the vertical jumps shown in Fig. 3 of the main text, Fig. S14.C and Fig. S15. If a Fermi level μ is introduced close enough to the energy of a WP (or WP group for that matter), such that the linear dispersion still holds, the jumps get modified:

$$c_{\text{WP}}(k_z) = \chi_{\text{WP}} \Theta_{\mu}(k_z - k_{z,\text{WP}})$$

with

$$\Theta_{\mu}(k_z) = \text{sign}(k_z) \begin{cases} 1 & |\mu| < |k_z| \\ \frac{|k_z|}{|\mu|} & |k_z| < |\mu| \end{cases}$$

and μ measured relative to the degenerate point and k_z being scaled with a suitable band velocity (omitted). Here we integrated over the whole infinite k_x, k_y -plane. Finite integration over a disk of radius R modifies the expression but not in an essential way. The modification is due to the necessary omission ($\mu < 0$) or addition ($\mu > 0$) of a disk of radius μ around the planar WP position and holds for $\mu \leq 0$. The curve is essentially a step function with a linear rise of width $|\mu|$ instead of a vertical jump. The corresponding k_z -integral becomes

$$\Delta\sigma_{xy}(k_z) \propto \chi_{\text{WP}} \Delta\sigma_{\mu}(k_z - k_{z,\text{WP}})$$

$$\Delta\sigma_{\mu}(k_z) = \begin{cases} 0 & k_z < -|\mu| \\ \frac{(k_z + |\mu|)^2}{4|\mu|} & |k_z| < |\mu| \\ k_z & |\mu| < k_z \end{cases}$$

which for k_z above $k_{z,\text{WP}} + \mu$ gives the same total contribution of a WP group as eq. S9. The result is altered locally around the groups k_z -position but far away the AHC signal is Fermi level independent (see also [30]). This is of course only true if the ideal linear Weyl dispersion holds and if the broadening due to the linear sections does not become comparable to the size of the total k_z -interval. Interestingly, numerical results for Fermi levels close to a twelve-fold groups energy show a $c(k_z)$ signal of the group, which looks very similar to the idealized results derived here. For larger energy distances we see more and more deviations from the ideal behavior.

Fig. S14.D is the equivalent of Fig. S14.C for $\mu = E_F = 45.3\text{meV}$. Note, how the vertical jumps become linearly interpolated jumps. The linear regions of the two contributions around the middle of the k_z -axis are quite narrow, since these WPs have an energy close to μ , while the other four WPs have larger deviations of their energy from μ and hence wider linear regions. The resulting $\Delta\sigma_{xy}(k_z)$ signal looks quite different from the constant homo case but its total value for large k_z is Fermi level independent.

In a real band structure the ideal WP linear dispersion bends into the real bands away from the WP position, which partially removes the Fermi level independence and leads to the washing out of the effects of the integer Chern numbers. Additionally, some of the WPs are highly anisotropic, which leads to further deviations from the idealized model discussed above.

This Fermi level independence gets also altered if the Weyl points are of type II, in which case the formulas above need to be modified and additionally the associated Fermi pockets, especially if they are small, quickly lead to a deviation from an ideal Weyl Hamiltonian.

S11. Band 47

Unsurprisingly, the magnetic field also induces Weyl points in other bands. For k_z -values between 0.17 and 0.5 there are several Fermi surface sheets and hence the focus on the integer contribution of band 48 (which is the homo for the originally discussed Weyl point group (G_3^{48})) is not justified, especially for the peaks P_1 at $k_z \approx 0.27$, P_2 at $k_z \approx 0.38$ and P_3 at $k_z \approx 0.43$, which give the largest contribution to the AHC signal (black curve in Fig. 3 and Fig. S16.A,B).

We hence have to analyze band 47 as well. It turns out that there are 11 Weyl point groups, which all are at least partially type II. All groups seem to be associated with nodal lines (See Fig. S16.C). Some contain only two or four Weyl points while the rest are six-fold, which means that all but the four-fold groups are uncompensated contributing an effective jump of the Chern number by ± 1 . The groups with less than six points are consistent with the numerical plaquette type results (green curve in Fig. S16.B), which does however not exclude the possibility that we missed some Weyl points, which form compensating pairs and hence do not show in the numerical results at least in the used resolution.

Groups $G_{5\dots 10}^{47}$ have energies between -100 and +125 meV. Fig. S16.AB show the comparison between the integer Chern signals for an assumed constant homo 48 and 47 as well as $c(k_z, E_F = 45.3\text{meV})$ and the resulting AHC signal. Groups $G_{1\dots 4}^{47}$ have $k_z < 0.15$ and hence lay in the region where band 48 is the homo. Consequently, their Weyl points are fully occupied and the integer Chern signal is not realized if a Fermi energy is included.

Since, the groups mostly contain type II Weyl points the simple argument of energy independence of the AHC signal (for an ideal Weyl Hamiltonian) does probably hold to a lesser extend. The inevitable associated Fermi pockets lead to a quick deviation from the ideal case. It is therefore better to explain the large peaks $P_{1,2,3}$ of $c(k_z, E_F = 45.3\text{meV})$ via close by Weyl points. We managed to attribute peak P_2 at $k_z \approx 0.38$ (and probably also peak P_3 at $k_z \approx 0.43$) to the sixfold group G_8^{47} of band 47, which has Weyl point energies $+66 \dots +91$ meV. Fig. S17.A-C show the contribution $c(k_{x,y}, k_z)$ to the Chern signal $c(k_z)$ for the chosen Fermi energy of 45.3meV for three k_z -values in the upper panels and the highest occupied bands as function of $k_{x,y}$ for this Fermi level in the lower panel. The type II Weyl points of G_8^{47} are marked by red (positive chirality) and blue (negative chirality) pluses.

Fig. S17.D shows corresponding data at the approximate Weyl point position $k_z = 0.338$ and energy 78.5meV of G_8^{47} . The Weyl points sit where the pockets of band 48 touch the border between bands 46 and 47, which is a signature of a type II Weyl point. At these parameters no big Berry curvature can be seen. If we lower the energy to 45.3meV and shift k_z to 0.36 (Fig. S17.A) the pockets of band 48 get smaller and have nearly vanished for $k_z = 0.373$ (close to the maximum of peak P_2), while at the same time Berry curvature gets induced at this very spot. For illustration the positions of the Weyl points of G_8^{47} are depicted in Fig. S17.E in the first BZ. They all lay close to a mirror plane (solid lines) and nodal lines.

Apparently, Weyl points need not be close in k_z - E -position to where the Berry curvature acquires a sizable signal. For peak P_1 we can establish a (linear) path through k_z - E -space from the position of the maximum of P_1 (Fig. S18.A) to the approximate Weyl point position (Fig. S18.G) of G_{10}^{47} ($k_z \approx 0.325$, $E = 130\text{meV}$), along which the topology of the Fermi surface sheets changes little, which makes the attribution of the Berry curvature of peak P_1 to group G_{10}^{47} likely. Since the WPs of G_{10}^{47} are not sitting at the exact same k_z and energy the Lifshitz transitions of the associated pockets (type II Weyl points) are not happening simultaneously along the path. Nevertheless, the transitions are clearly discernable. Note, that the WP chirality is opposite to the sign of the Berry curvature maxima. This is a consequence of the jump of χ at the WP position as a function of k_z . Depending on which side of the WP one takes a cut the sign of the Berry curvature pattern switches. It should also be noted that the Berry curvature towards the end of the path (Fig. S18.I), has the same Berry curvature sign pattern at the WPs as the WP's chirality, however with sizable Berry curvature in the triangular area close to $k_{x,y} = 0$. The symmetry of the curvature in this area seems to approximately follow the full \mathcal{C}_{3v} symmetry (as opposed to the curvature at the WPs) and hence largely integrates to a small total signal.

It turns out that G_5^{47} has Weyl point position at very similar $k_{x,y}$ as G_{10}^{47} but at $k_z \approx 0.168$ and $E \approx -98\text{meV}$. However, in this case the Fermi surface sheets evolve into a completely different topology (Fig. S19). Again the Berry curvature pattern changes sign when going through the WPs, only this time the chirality pattern coincides with the BC pattern at peak P_1 , which is due to the fact that G_5^{47} has an effective positive jump of the integer Chern number. Indeed the pockets between bands 46 and 47 are the positions which yield the BC maxima.

S12. Lattice structure

We used space group 157 (P31m) with lattice parameters $a = b = 6.57316\text{\AA}$ and $c = 6.16189\text{\AA}$. The Wyckoff positions are: Pt at (0.2619, 0, 0.004), Bi_1 at (0, 0, -0.359), Bi_2 at $(\frac{2}{3}, \frac{1}{3}, -0.204)$ and Bi_3 at (-0.3856, 0, 0.271).

S13. TNL conversion into Weyl Nodes: Model Hamiltonian

Our starting point is a $\mathbf{k} \cdot \mathbf{p}$ model for two nodal loops centered around two valleys $\Lambda_{1,2}$ related by time-reversal symmetry and located on a mirror invariant plane, which, as in the main part of the manuscript, we take as $k_x \equiv 0$. The corresponding vertical mirror symmetry can be represented as $\mathcal{M}_x = -i\sigma_x \otimes \tau_0$ with the Pauli matrix vectors $\boldsymbol{\sigma}$ and $\boldsymbol{\tau}$ that act in spin and valley space respectively. Since time-reversal symmetry exchanges the two valleys, it can be represented as $\Theta = -i\sigma_y \otimes \tau_x$. We next introduce a two band model Hamiltonian, which generalizes the model considered in Ref.[16], that respects time-reversal and mirror symmetry and reads:

$$\mathcal{H}_{\mathbf{k},\mathbf{p}} = \alpha k_x k_y \sigma_z \otimes \tau_z + \alpha k_x k_z \sigma_y \otimes \tau_z + \beta (k_0^2 + k_x^2 - k_y^2 - k_z^2) \sigma_x \otimes \tau_z. \quad (\text{S10})$$

For $k_x \equiv 0$ two circular nodal loops of radius k_0 are obtained. We next consider the effect of a planar magnetic field introducing a Zeeman coupling

$$\mathcal{H}_{Zeeman} = B \cos \theta \sigma_x \otimes \tau_0 + B \sin \theta \sigma_y \otimes \tau_0 \quad (\text{S11})$$

where θ indicates the angle of the planar magnetic field from the \hat{x} direction. It is instructive to first consider the effect of a magnetic field with $\theta \equiv 0$, in which case the vertical mirror symmetry is preserved. For small enough (positive) values of the magnetic field, one finds that the nodal line in one valley expands – its radius is renormalized by the magnetic field to $\sqrt{k_0^2 + B}$ – while the nodal line in the opposite valley get shrunk to a radius $\sqrt{k_0^2 - B}$. At the critical value of magnetic field $B_c \equiv k_0^2$ the nodal line shrinks to a single point (see Figure S20.a). It is at this critical magnetic field that the conversion of the nodal line into Weyl points occurs. For $B > B_c$ zero energy states are in fact obtained at $k_y \equiv k_z \equiv 0$ and at the two mirror symmetry related momenta $k_x \equiv \pm\sqrt{B - k_0^2}$ (see Figure S20.a). The conversion by a mirror symmetry preserving planar magnetic field is therefore “local” in momentum space: a nodal line shrinks to a single point out of which two Weyl nodes of opposite chirality emerge.

The conversion of a nodal line into Weyl nodes is instead completely different in nature when considering a planar magnetic field that breaks the protecting vertical mirror symmetry. It in fact occurs even for infinitesimal B values. Let us take the planar magnetic field to be parallel to the vertical mirror plane and therefore oriented along the \hat{y} direction. We thus set $\theta = \pi/2$ in the Zeemann Hamiltonian above. Using that the Hamiltonian is diagonal in valley space, the eigenenergies can be then written as

$$E^2 = \alpha^2 k_x^2 k_y^2 + (\alpha k_x k_z \pm B)^2 + \beta^2 (k_0^2 + k_x^2 - k_y^2 - k_z^2)^2 \quad (\text{S12})$$

where \pm distinguishes the two valleys. The spectrum is symmetric under $E \rightarrow -E$. Therefore, Weyl nodes, if present, will appear as zero-energy states. These are determined by requiring that the three squared polynomials in the equation above must simultaneously vanish. From the first term on the r.h.s. of the equation above we immediately have that the Weyl nodes will sit on the $k_y \equiv 0$ plane. The two constraints $\alpha k_x k_z \pm B \equiv 0$ and $k_0^2 + k_x^2 - k_z^2 \equiv 0$ determine the complete position of two Weyl nodes per valley. We note that since the combined \mathcal{M}'_x point group symmetry is preserved the Weyl nodes in opposite valleys are paired up to have opposite k_z values and equal k_x values. This results are sketched in Figure S20.c. For $B \rightarrow 0$ we find that the Weyl nodes appear at $k_x \simeq 0$ and $k_z \simeq \pm k_0$. In other words, Weyl nodes emerge out of a nodal loop with a k_z distance that equals the nodal loop radius. This highlights the “non-local” conversion of nodal loops into Weyl nodes.

S14. TNL gap in magnetic field and thermal activation

It is possible to estimate the size of the gap at the onset field $B_{ons} = 2.8$ T by considering that it equates the thermal energy: $-g\mu_B m B_{ons} = k_B T$ (with $m = \pm 1/2$ for electrons). For this, we must assume a value of the g-factor. With a g-factor of 6 for band 28 (from [31]), we get $-g\mu_B m B_{ons} \sim 486 \mu\text{eV}$, which is very consistent with $k_B T \sim 430 \mu\text{eV}$ at $T = 5$ K.

We can compare this to the TNL gap from DFT calculations performed for Zeeman energies $E_Z = 500 \mu\text{eV}$ and $E_Z = 1\text{meV}$, although some important precautions must be taken when comparing the two, as we will detail later. Figure S21 shows the points considered along the TNL in (a) and the gap along the TNL at both Zeeman energies in (b). The TNL is already gaped by about $500 \mu\text{eV}$ in some places at $E_Z = 500 \mu\text{eV}$, while at $E_Z = 1\text{meV}$ almost the entire TNL is gaped by more than $500 \mu\text{eV}$. This is consistent with the small calculation shown above.

This DFT calculation cannot however be directly compared to the real system for two reasons: First, the points shown are in the mirror plane \mathcal{M}_x , while the WNs do not lie in the plane (they move in the k_x direction under the magnetic field). Second, the TNL does not sit exactly at E_F , nor is it at a constant energy, meaning the temperature does not have the same effect in all parts of the TNL.

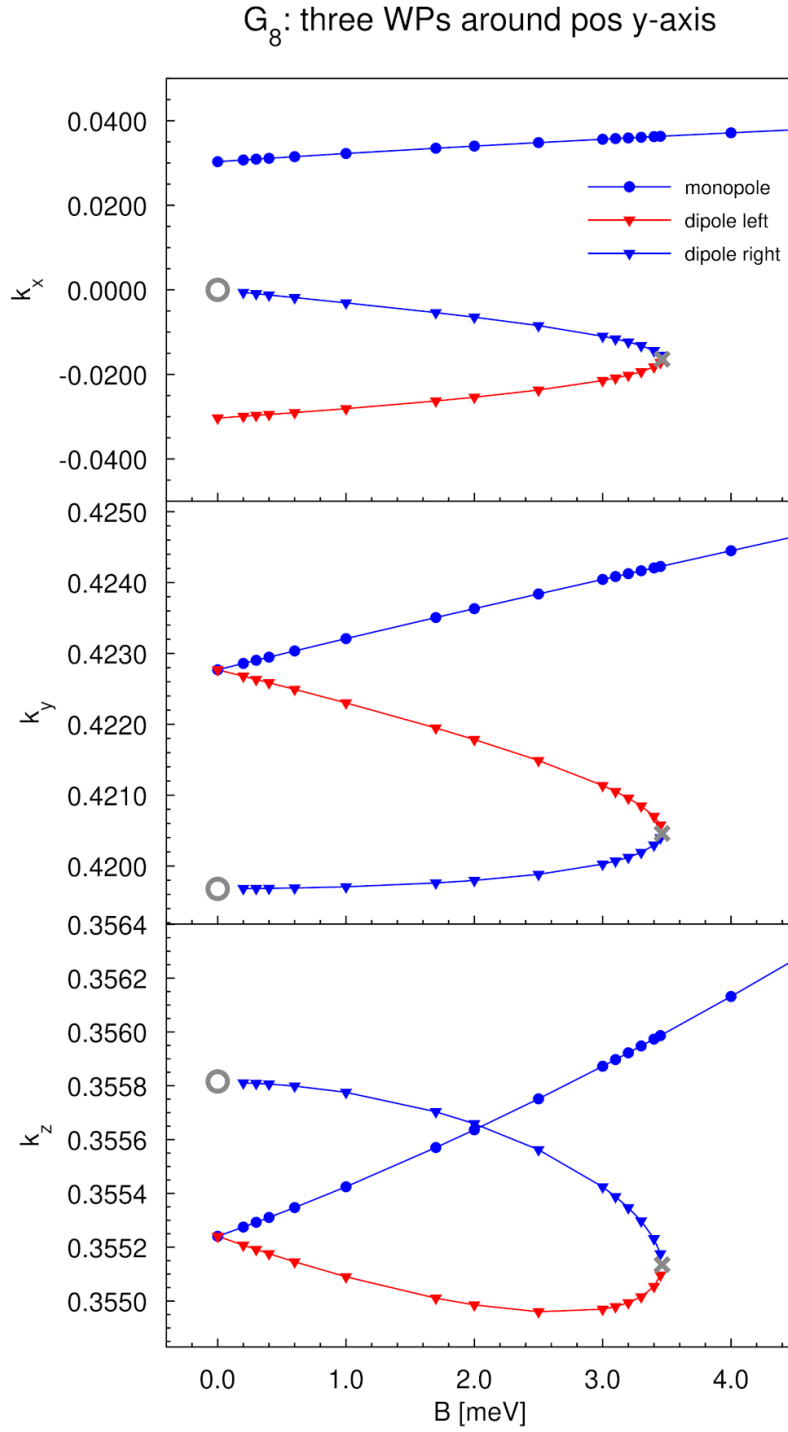


Figure S13. Evolution of the three WPs close to the positive y -axis of G_8^{48} for small magnetic fields. The open circle denotes the position at which one of the WPs dissolves into the nodal loop. At $B = 0.35$ a dipole emerges at negative k_x (gray cross). Compare to last row of Fig. S12.

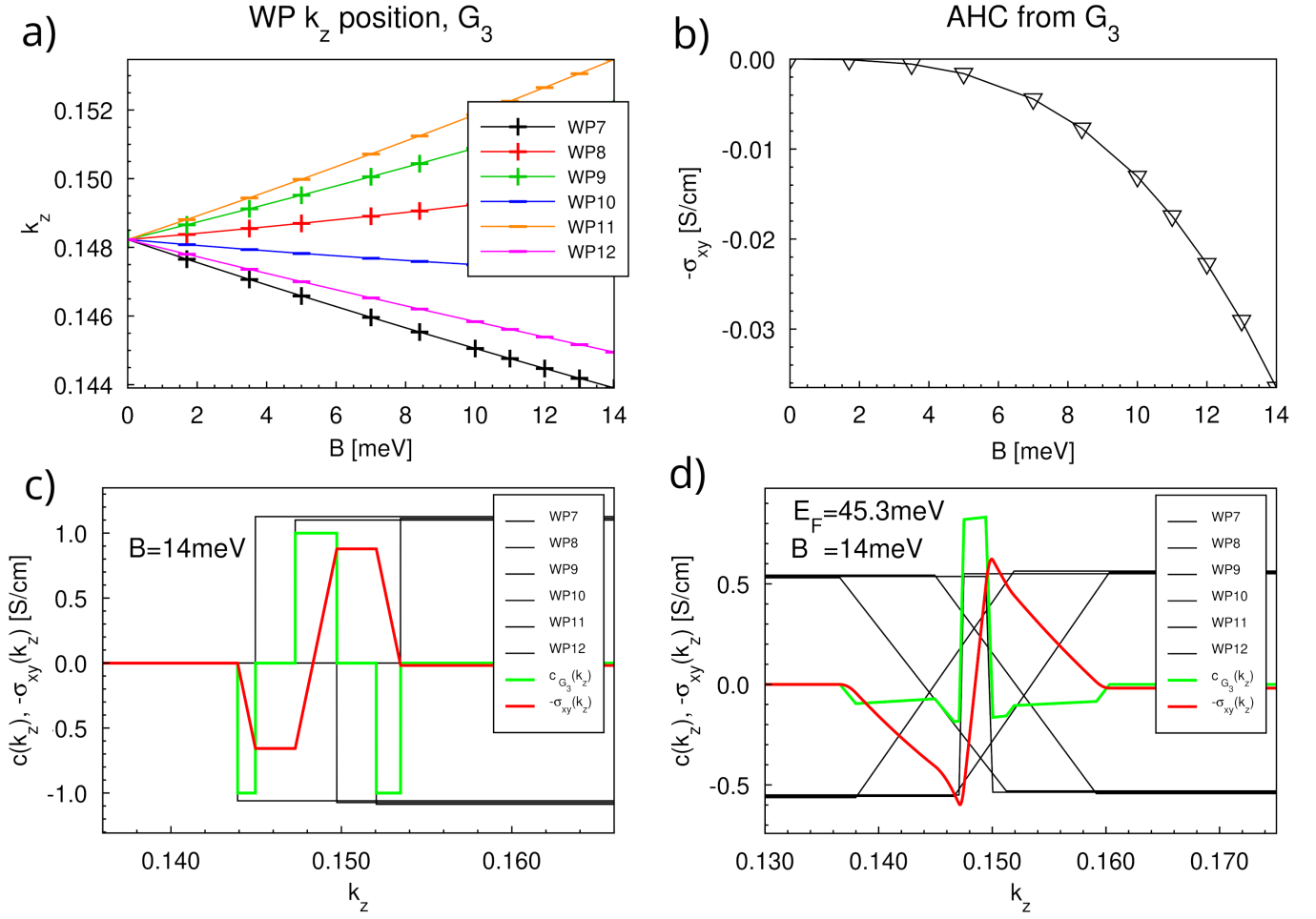


Figure S14. a) the evolution of the WP k_z -position of the six WP with $k_z > 0$ of G_3^{48} as a function of B . The plus/minus symbols denote the chirality. b) The resulting AHC signal for the fully linearly compensated group G_3^{48} as a function of field B assuming ideal Weyl dispersion. c) The individual contributions (jumps) due to the six $k_z > 0$ WPs of G_3^{48} (black) offset along the y -axis for better visibility, their sum $c(k_z)$ and its k_z -integral $-\Delta\sigma_{xy}(k_z)$ in S/cm (red). d) As c) but for $E_F = 45.3 \text{ meV}$.

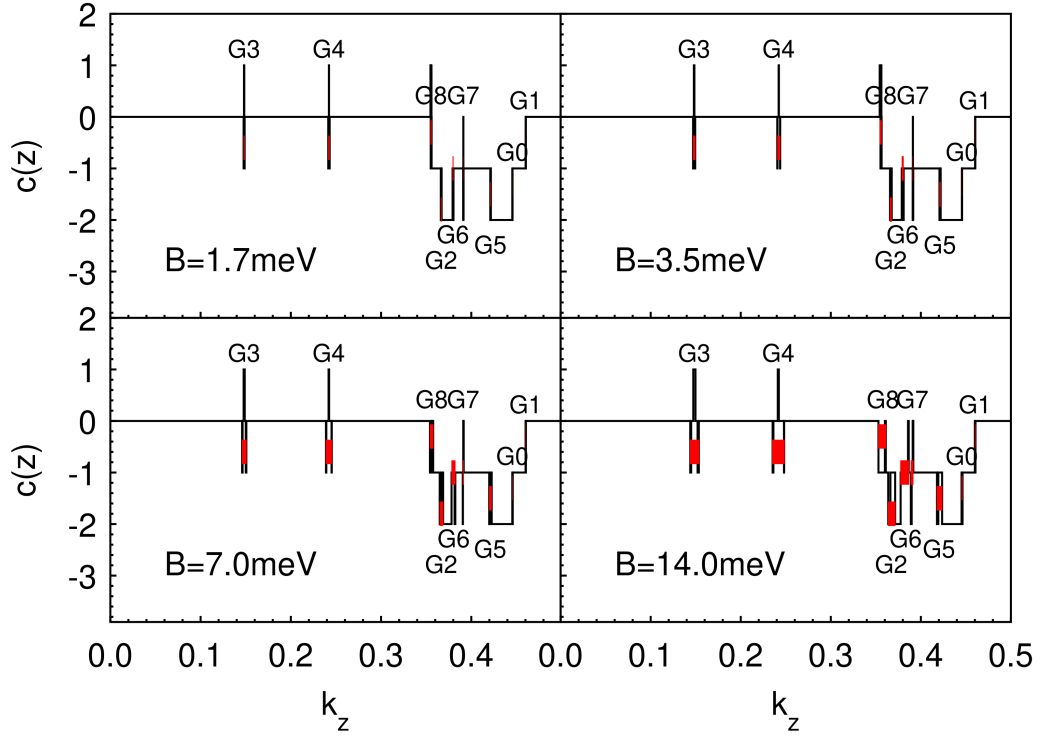


Figure S15. Chern signal $c(k_z)$ for four magnetic fields for constant homo 48. The jumps are labeled by the corresponding WP groups. The red bars span all WPs of the corresponding group.

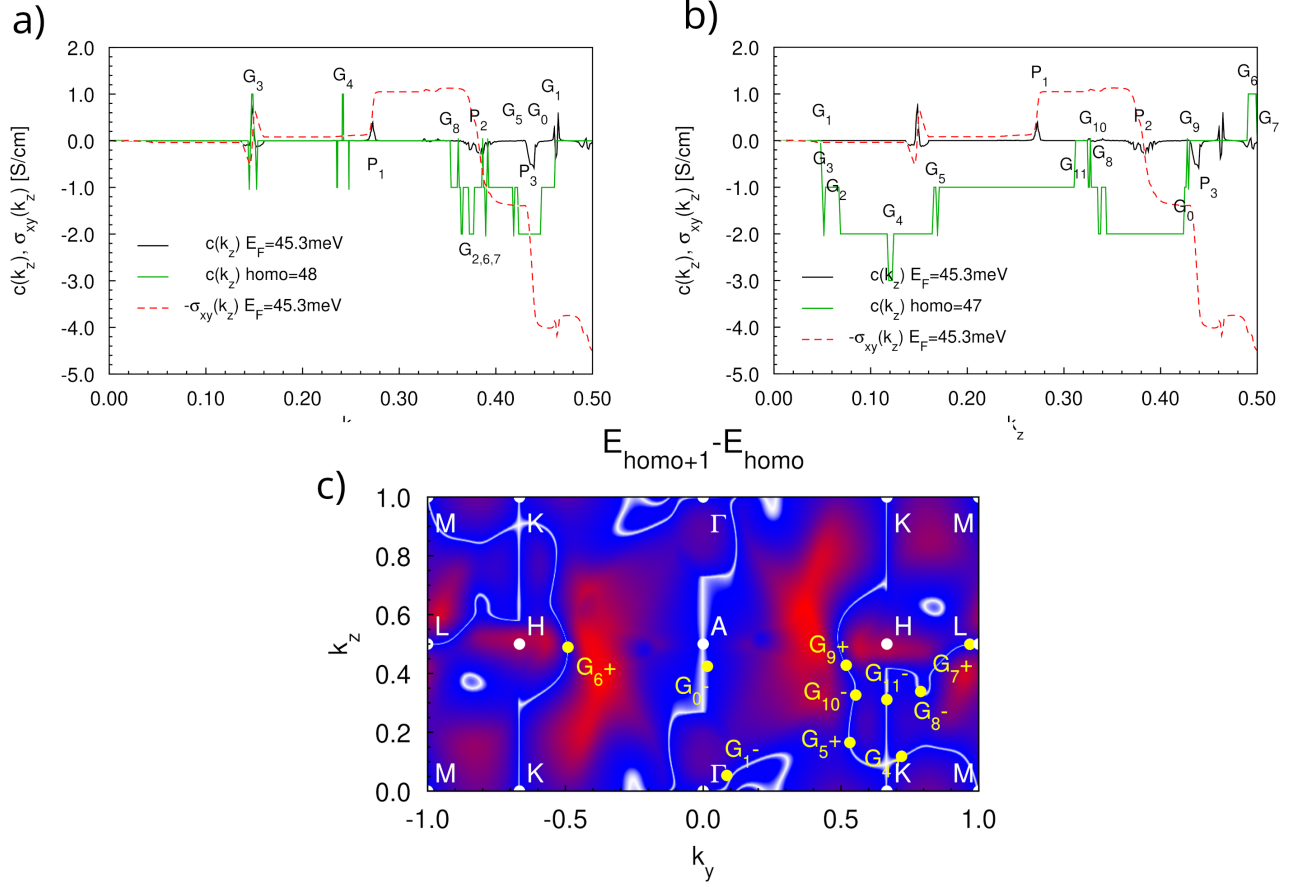


Figure S16. **a,b**: the k_z -resolved Chern number for (green) constant homo, (black) constant Fermi energy and (red-dashed) the resulting AHC signal $-\Delta\sigma_{xy}(k_z)$ for **a**: homo 48 and **b**: homo 47. **c**: the Energy gap for homo 47. White denotes zero gap (nodal lines). All groups except $G_{2,3}^{47}$ are shown and fall close the nodal lines. $G_{2,3}^{47}$ are two-point groups and are closer to other mirror planes and hence do not fit into this picture.

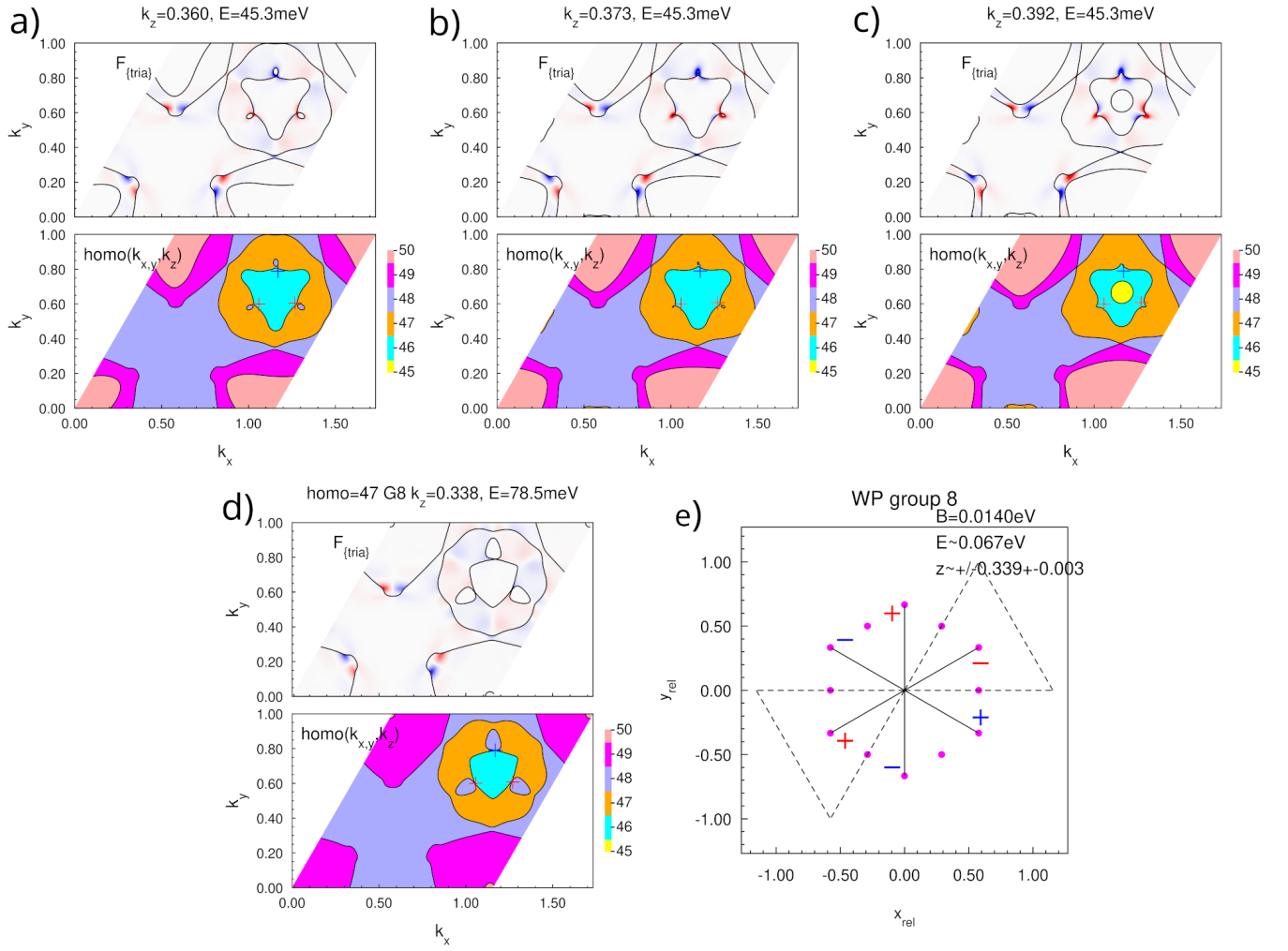


Figure S17. **a-c:** $c(k_x, y, k_z)$ (upper panel) and $\text{homo}(k_x, y, k_z)$ (lower panel) for the peak P_2 at Fermi energy 45.3meV for three k_z values. **d:** Same data as in **a-c** at k_z and E of the sixfold group G_8^{47} . **e:** The arrangement of the Weyl points of G_8^{47} . The Weyl points are marked with pluses, their chirality with red(positive) or blue(negative) color.

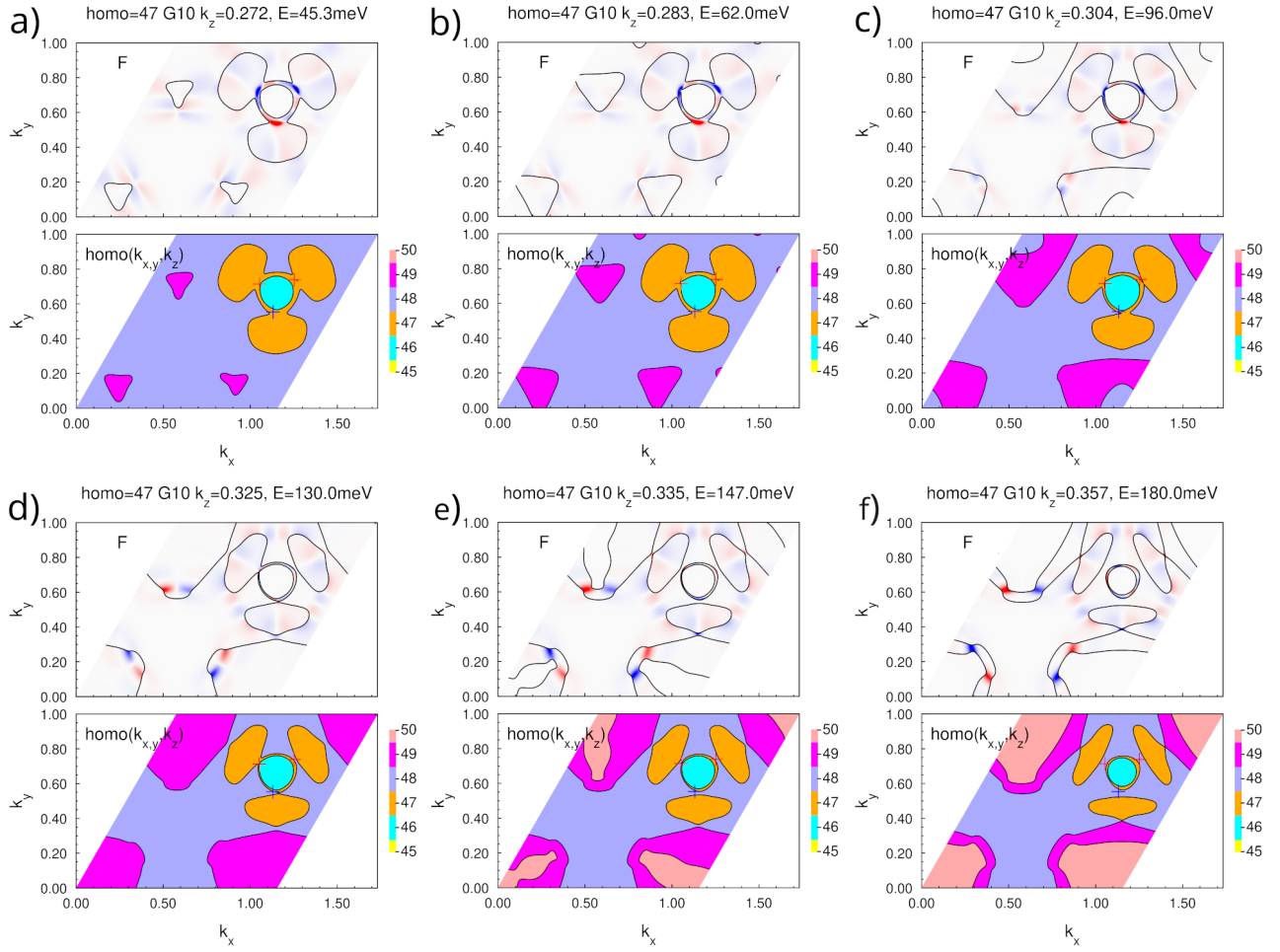


Figure S18. Peak P_1 . **a**: $c(k_{x,y}, k_z)$ and homo structure for $k_z = 0.272$ and $E_F = 45.3\text{meV}$ (maximum of P_1). **b . . . i**: evolution of $c(\mathbf{k})$ along a linear path in k_z and E from P_1 (**a**) through the approximate WP k_z - and E -position of G_{10}^{47} (**d**) up to a position on the other side of the WP position (**f**), with chirality indicated by red(positive) and blue(negative) color resp.

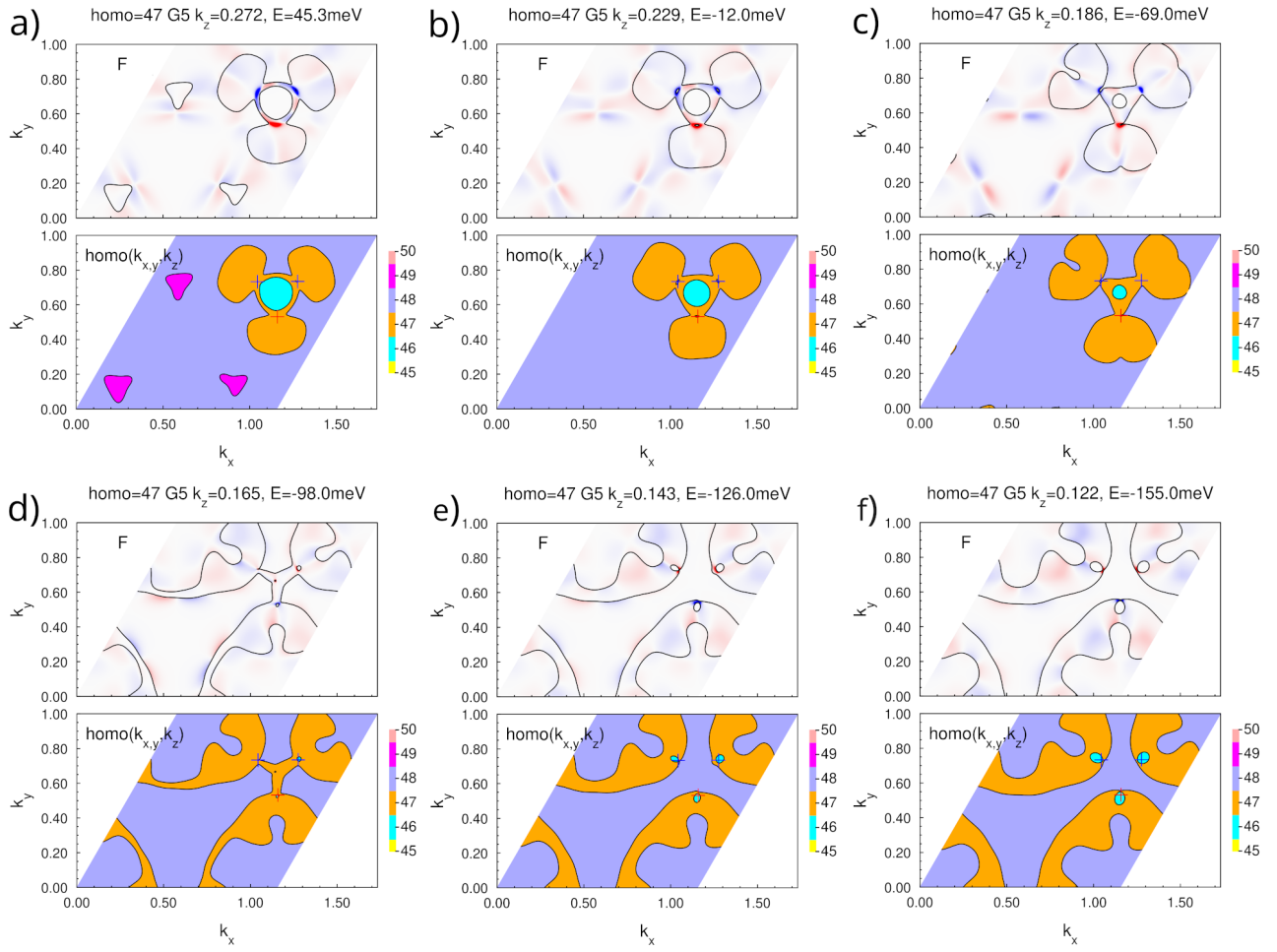


Figure S19. Peak P₁. **a**: $c(k_{x,y}, k_z)$ and homo structure for $k_z = 0.272$ and $E_F = 45.3\text{meV}$ (maximum of peak P₁). **b**...**f**: evolution of $c(\mathbf{k})$ along a linear path in k_z and E from peak P₁ (a) through the approximate WP k_z - and E -position of G_5^{47} (d) up to a position on the other side of the WP position (f). Pluses mark the position of the WPs, with chirality indicated by red(positive) and blue(negative) color, resp.

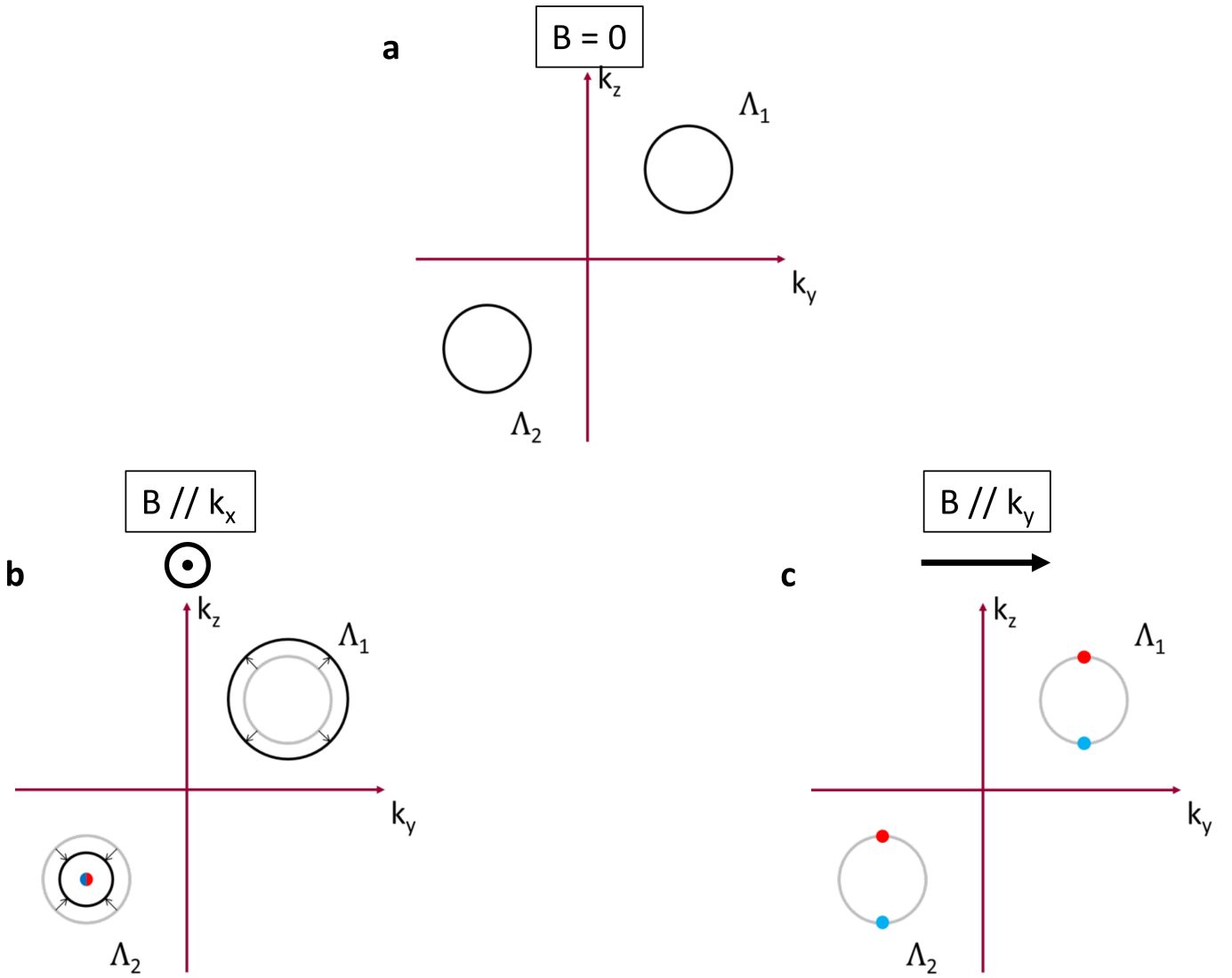


Figure S20. Toy model showing the position of the Weyl nodes (originating from the TNL) as a function of a magnetic field which either preserves the \mathcal{M}_x mirror symmetry (a), or breaks that mirror symmetry (b,c). In each graph, the positions of the two Weyl nodes of opposite chiralities are shown in blue and red, respectively. All WNs always sit in the $k_y = 0$ plane. (a) shows the k_x position of the two WNs when the field is along k_x . In this case, both WNs are always at $k_z = 0$. It can be seen that the two WNs originate from the same point at $k_x = 0$ when the field reaches the critical value. (b,c) show the k_x and k_z positions, respectively, of the two WNs when the field is along k_y . As soon as $B > 0$, two WNs appear at $k_x = 0$ and $k_z = \pm 1$, and start drifting in magnetic field. This shows the non-local nature of the WN creation from TNLs.

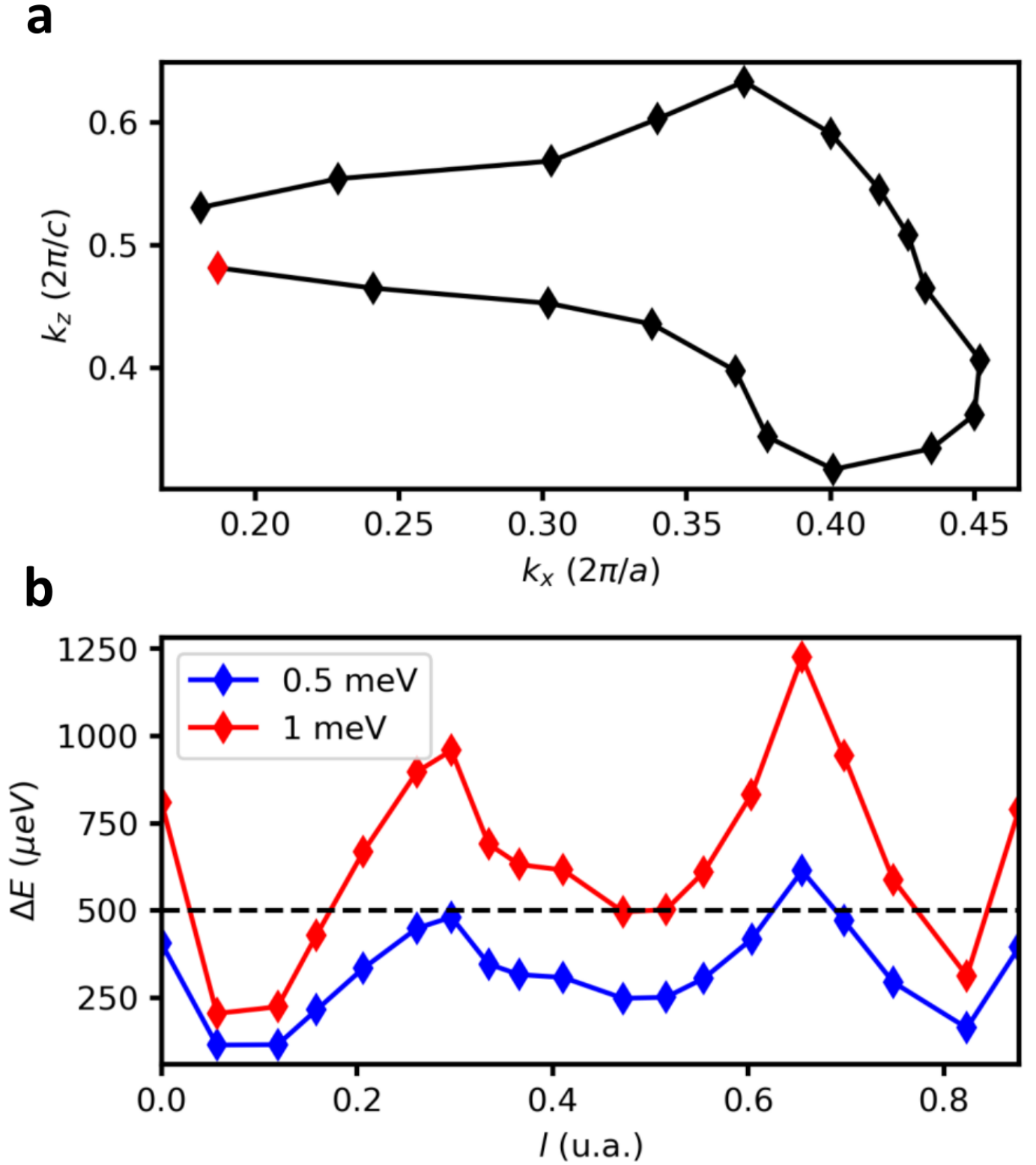


Figure S21. DFT calculation of the gap opening in field at different points along the TNL. (a) Black diamonds: (k_x, k_z) positions of the different points considered along the TNL (in the mirror plane \mathcal{M}_x); Red diamond: First point considered when going along the TNL. (b) Size of the gap along the TNL, for two Zeeman energies (0.5 meV in blue, and 1 meV in red). The parameter l corresponds to the length along the path going through all points in (a), starting from the red diamond.